HHS Public Access

Author manuscript

Cell Rep. Author manuscript; available in PMC 2022 March 12.

Published in final edited form as:

Cell Rep. 2022 February 01; 38(5): 110323. doi:10.1016/j.celrep.2022.110323.

SIX1 reprograms myogenic transcription factors to maintain the rhabdomyosarcoma undifferentiated state

Jessica Y. Hsu[1,2], **Etienne P. Danis**[1,11], **Stephanie Nance**[9], **Jenean H. O'Brien**[4], **Annika L. Gustafson**[1,3], **Veronica M. Wessells**[5], **Andrew E. Goodspeed**[1,11], **Jared C. Talbot**[6], **Sharon L. Amacher**[7], **Paul Jedlicka**[8], **Joshua C. Black**[1,2], **James C. Costello**[1,2,11], **Adam D. Durbin**[9], **Kristin B. Artinger**[10,11,*], **Heide L. Ford**[1,2,11,12,*]

[1]Department of Pharmacology, University of Colorado Anschutz Medical Campus (UC-AMC), Aurora, CO, USA

[2]Pharmacology Graduate Program, UC-AMC, Aurora, CO, USA

[3]Molecular Biology Graduate Program, UC-AMC, Aurora, CO, USA

[4]Department of Biology, College of St. Scholastica, Duluth, MN, USA

[5]Division of Medical Oncology, UC-AMC, Aurora, CO, USA

[6]School of Biology and Ecology, University of Maine, Orono, ME, USA

[7]Department of Molecular Genetics, Ohio State University, Columbus, OH, USA

[8]Department of Pathology, UC-AMC, Aurora, CO, USA

[9]Division of Molecular Oncology, St. Jude Children's Research Hospital, Memphis, TN, USA

[10]Department of Craniofacial Biology, UC-AMC, Aurora, CO, USA

[11]University of Colorado Cancer Center, UC-AMC, Aurora, CO, USA

[12]Lead contact

SUMMARY

Rhabdomyosarcoma (RMS) is a pediatric muscle sarcoma characterized by expression of the myogenic line-age transcription factors (TFs) MYOD1 and MYOG. Despite high expression of these TFs, RMS cells fail to terminally differentiate, suggesting the presence of factors that alter

*Correspondence: heide.ford@cuanschutz.edu (H.L.F.), kristin.artinger@cuanschutz.edu (K.B.A.).

AUTHOR CONTRIBUTIONS

K.B.A. and H.L.F. conceptualized and supervised experiments with input from A.D.D., J.C.B., and J.C.C. J.Y.H., S.N., and A.L.G. performed cell line experiments and were involved in data generation and interpretation. J.Y.H. performed mouse experiments. J.Y.H. and J.H.O. performed zebrafish experiments. J.Y.H., S.N., E.P.D., and A.E.G. performed and analyzed NGS experiments. V.M.W. and P.J. performed and scored tumor histology in zebrafish and mouse models. Critical reagents were provided by S.L.A., A.D.D., and J.T. J.Y.H. wrote the manuscript with significant input from K.B.A., H.L.F., A.D.D., J.C.B., and J.C.T. All authors contributed to manuscript editing and review.

SUPPLEMENTAL INFORMATION

Supplemental information can be found online at https://doi.org/10.1016/j.celrep.2022.110323.

DECLARATION OF INTERESTS

J.C.C. is a co-founder of PrecisionProfile. H.L.F. is a co-founder of Sieyax, LLC.

their functions. Here, we demonstrate that the developmental TF SIX1 is highly expressed in RMS and critical for maintaining a muscle progenitor-like state. SIX1 loss induces differentiation of RMS cells into myotube-like cells and impedes tumor growth *in vivo*. We show that SIX1 maintains the RMS undifferentiated state by controlling enhancer activity and MYOD1 occupancy at loci more permissive to tumor growth over muscle differentiation. Finally, we demonstrate that a gene signature derived from SIX1 loss correlates with differentiation status and predicts RMS progression in human disease. Our findings demonstrate a master regulatory role of SIX1 in repression of RMS differentiation via genome-wide alterations in MYOD1 and MYOG-mediated transcription.

Graphical abstract

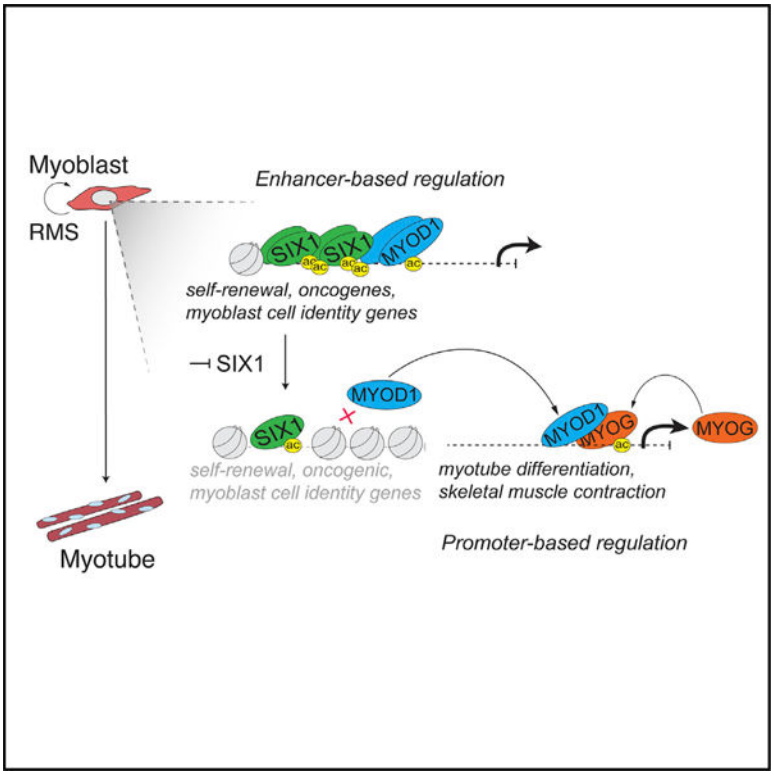

In brief

Hsu et al. demonstrate that the developmental transcription factor SIX1 is highly expressed in rhabdomyosarcoma and critical for maintaining a muscle progenitor state via regulation of MYOD1 and MYOG binding accessibility at critical loci governing myogenic cell fate.

INTRODUCTION

Rhabdomyosarcoma (RMS) is a soft-tissue pediatric sarcoma with molecular and histological features that resemble undifferentiated skeletal muscle. The majority of pediatric RMS cases can be divided into two major subtypes, embryonal RMS (ERMS) and alveolar RMS (ARMS), which are designated based on their histology. Although ERMS

tumors are characterized by a variety of mutational events, notably *RAS* mutations, ARMS tumors are associated with PAX3-FOXO1 or PAX7-FOXO1 chromosomal rearrangements, which has led to replacement of the histological annotations ERMS and ARMS with "fusion-negative (FN)" and "fusion-positive (FP)". The distinct genetic perturbations associated with ERMS and ARMS have long implied that the RMS subtypes arise from distinct mechanisms; however, a shared feature of all RMS tumors is their expression of the myogenic regulatory transcription factors (TFs) *MYOD1* and *MYOG*, orchestrators of skeletal muscle differentiation with aberrant functions in RMS (Rekhi et al., 2018). Although, in normal skeletal muscle differentiation, these myogenic TFs coordinate the expansion, commitment, and eventual differentiation of embryonic mesodermal or myogenic progenitors, expression of these myogenic TFs in RMS tumors is not coupled with exit from the cell cycle and differentiation into post-mitotic myofibers (Weintraub et al., 1989). Several studies have discovered distinct activities of these myogenic TFs in the context of normal muscle development and RMS (Londhe and Davie, 2011; MacQuarrie et al., 2013; Yang et al., 2009). However, it remains less clear what factors cause these myogenic regulatory factors (MRFs) to depart from their canonical roles as drivers of muscle differentiation to instead maintain RMS cells as less differentiated muscle progenitors.

The *SIX1* homeodomain-containing TF belongs to the *Six* family, which includes *SIX1–SIX6* in vertebrates. Early studies of the *SIX1* ortholog in *Drosophila*, *sine oculis* (*so*), placed the functions of the *Six* gene family in eye morphogenesis because *so* mutants lack compound eye structures (Cheyette et al., 1994). However, *Six* genes are now known to operate beyond the visual system in invertebrates and vertebrates (Dubois et al., 2016). Notably, the mammalian orthologs *Six1* and *Six4* have conserved and indispensable roles in embryonic skeletal muscle development and skeletal muscle regeneration. In mice, *Six1* deficiency causes reduced and disorganized muscle mass (Laclef et al., 2003), and further ablation of its ortholog, *Six4*, causes exacerbated craniofacial defects and severe muscle hypoplasia (Grifone et al., 2005). In *Six1*- and *Six1/Six4*-deficient mouse models, expression of the critical myogenic TFs *MYOD1* and *MYOG* is compromised in migrating hypaxial muscle, demonstrating that *Six1* and *Six4* are required for activation of these myogenic TFs to induce muscle differentiation. In zebrafish, morpholino-mediated loss of *six1b* gene expression similarly causes reduced hypaxial muscle and impairment of *Pax7+* muscle stem cell proliferation during skeletal muscle repair (Lin et al., 2009; Nord et al., 2013). Recently, genetic ablation of *six1a/six1b/six4a/six4b* paralogs in the zebrafish genome has additionally shown that compound loss of *six1/4* function causes complete loss of all migratory muscle precursors that generate hypaxial muscles, such as the fin muscles, while leaving trunk muscles relatively unaffected (Talbot et al., 2019). These results align with previous observations that morpholino-mediated loss of *six1a* and *six1b* also affect hypaxial muscles, although the muscle defects observed in the morpholino studies are more severe than those seen in the *six1a/six1b* genetic mutant (Lin et al., 2009; Nord et al., 2013; Talbot et al., 2019). These studies demonstrate that *Six1*, which acts in concert with *Six4*, lies upstream of the myogenic specification gene regulatory network and is a necessary component of the skeletal muscle transcriptional circuit.

Myogenic differentiation is tightly governed by a cascade of MRF expression, which encompass the highly conserved class II basic-helix-loop-helix (bHLH) TFs *MYOD1*,

MYF5, *MYOG*, and *MRF4*. During the course of embryonic development as well as skeletal muscle repair and regeneration, these four MRFs are considered necessary for committing progenitor cells to the skeletal muscle lineage, expanding the progenitor cell pool, and differentiating committed cells into contractile muscle fibers (Zammit, 2017). Although structurally the MRF family is conserved, the transition of muscle progenitors from commitment to growth and, subsequently, to differentiation invokes subfunctionalized and context-specific roles of these MRFs. Indeed, *MyoD1* can activate distinct myoblast-specific and differentiation-specific gene expression programs by modifying chromatin environments that facilitate differentiation or myoblast growth (Cao et al., 2010; Soleimani et al., 2012). Because the functions of *MYOD1* are co-opted in RMS to foster growth rather than to promote differentiation, we hypothesized that other factors critical for normal skeletal muscle development must repress the differentiation subprograms of *MYOD1*. Given the role of *SIX1* in regulating upstream activities of *MYOD1* and *MYOG* to induce skeletal muscle development (Grifone et al., 2005; Liu et al., 2013; Menuet et al., 2002; Nord et al., 2013; Relaix et al., 2013; Santolini et al., 2016; Spitz et al., 1998), we sought to investigate the molecular functions of *SIX1* in regulating RMS progression. Although previous studies have identified *SIX1* as a driver of RMS progression (Yu et al., 2004, 2006), these studies largely attributed *SIX1*'s pro-metastatic activity to its transcriptional target, *EZR*. Here we report that SIX1 loss in RMS promotes cell cycle arrest and differentiation, contrasting its role in muscle development, where SIX1 loss is associated with failed differentiation (Wu et al., 2014). We show that high levels of SIX1 within RMS globally reprogram MYOD1 to occupy loci permissive to tumor growth instead of terminal muscle differentiation and that its loss restores the MYOD1/MYOG gene regulatory network that induces skeletal muscle differentiation.

RESULTS

SIX1 is overexpressed and predicted to be an essential gene in RMS

To examine whether SIX1 is highly expressed in human RMS, we interrogated its expression in publicly available RMS RNA sequencing (RNA-seq) datasets. In multiple independent datasets, high SIX1 mRNA expression could be detected compared with other sarcomas in the National Cancer Institute Oncogenomics pan-sarcoma dataset (Figure S1A) and the St. Jude Pediatric Cancer Genome Project (Figure S1B) and compared with normal tissue in the St. Jude Integrated RMS Database (iRDb) (Figure 1A). Notably, SIX1 was more highly expressed in RMS samples compared with muscle controls depicting different stages of skeletal muscle development (Figure 1A). We next assessed SIX1 protein expression in an RMS tissue array consisting of 96 human RMS samples and 8 normal skeletal muscle controls (Figures 1B and 1C). Using a 1–4 scoring system of nuclear immunohistochemistry staining, we detected strong nuclear SIX1 staining in ERMS and ARMS sections (18% and 29% with immunohistochemistry [IHC] staining scores of 2 or greater, respectively) compared with normal skeletal muscle control sections (0% with an IHC staining score of 2 or greater) (Figures 1B and 1C). To determine whether SIX1 has a functional role in RMS, we next examined data from the Broad Institute's exome-wide CRISPR-Cas9 knockout (KO) screen dataset (Dharia et al., 2021). In the 1,775 cell lines tested in the CRISPR-Cas9 screen, we observed that the 10 RMS cell lines used in the screen exhibited high SIX1

mRNA expression and high SIX1 gene dependency (Figure 1D). Further comparison of the RMS cell lines against all other tumor cell lines demonstrates that SIX1 is a selective dependency in RMS and is required for RMS cell survival ($q = 0.018$), as is the myogenic TF MYOD1 (Figure 1E).

To investigate SIX1 function in RMS, we examined expression of SIX1 in a panel of human RMS cell lines and detected high SIX1 expression in FN and FP RMS cell lines (Figure 1F). Although SIX1 expression is high in FP and FN RMS, we focused our studies on the FN subtype to interrogate the functions of SIX1 outside the context of the *PAX3-FOXO1* fusion, where it has already been demonstrated to be a downstream target of the fusion protein (Khan et al., 1999). Using two FN RMS cell lines (SMS-CTR and RD) that highly express SIX1, we sought to validate the CRISPR-Cas9 screen findings using an orthogonal method. We thus established SMS-CTR and RD cell lines transduced with shRNAs targeting no coding sequence in the genome (Scramble) or two distinct SIX1 sequences located in unique regions of the SIX1 C terminus or 3′UTR (SIX1 KD5 and KD6). We demonstrated that these shRNAs resulted specifically in SIX1 knockdown (KD) and did not decrease any other SIX family members (Figures 1G and S1C). In both cell lines, reduced levels of SIX1 resulted in deficits in cell growth and mitotic activity, as measured by IncuCyte live-cell growth assays (Figure 1H) and mitotic marker phospho-histone H3 (pH3) staining, respectively (Figure 1I). These data demonstrate that SIX1 is highly expressed and required for growth of RMS cells *in vitro*.

six1b is required for zebrafish RMS growth

Given the above *in vitro* observations, we sought to examine the role of SIX1 in an *in vivo* setting, first using a zebrafish model of ERMS (zRMS) induced by co-injection of the *rag2-kRASG12D* and *rag2-GFP* transgenes into the single-cell stage of the zebrafish (Langenau et al., 2007). This model results in generation of skeletal muscle tumors with histological features similar to human FN RMS and parallels our cell line data because SMS-CTR and RD cells are *RAS*-mutated FN RMS (Hinson et al., 2013; Sokolowski et al., 2014). To examine the expression of the two zebrafish *six1* paralogs *six1a* and *six1b* in zRMS tumors, we performed quantitative reverse-transcriptase PCR (qRT-PCR) and found that *six1b* was upregulated significantly in zRMS tissue compared with age-matched normal skeletal muscle (Figure 2A), which was confirmed using RNA *in situ* hybridization (ISH) (Figure 2B). To determine whether *six1b* was required for RMS growth *in vivo*, we then combined the zRMS injection model with zebrafish carrying genetic loss-of-function alleles for only *six1b* because of its more consistent overexpression in zRMS and because the *six1a*;*six1b* double mutant fails to survive to adult stages when zRMS tumors would form (Talbot et al., 2019). In contrast, *six1b* mutants develop normally and are therefore a suitable model to test the function of reduced *six1* levels in RMS *in vivo*. Consistent with previous findings, we found no differences in *pax3a*, *myod1*, or *myogenin* expression between wild-type and *six1b* mutant sibling embryos from the 5–20 + somite stages (Figures S2A–S2C; Talbot et al., 2019).

To determine whether *six1b* loss is sufficient to alter *kRAS*-mediated zRMS tumorigenesis, we injected *rag2-kRASG12D/GFP* transgenes into the progeny of *six1b*$^{+/-}$ breeding pairs

to generate age-matched sibling groups with all possible *six1b* genotypes. Interestingly, although GFP positivity could be detected in all genotypes, progression to overt tumors was largely lost with *six1b* depletion (Figures 2C–2E). We observed that tumors established in *six1b*$^{-/-}$ zebrafish grew significantly slower over a 120-day time course compared with tumors established in wild-type siblings (Figures 2C and 2D). Reflecting this reduced growth rate, *six1b*$^{-/-}$ tumors were smaller in size compared with wild-type siblings' tumors at their final collection time point 120 days post fertilization (dpf) (Figure 2E). IHC staining of tumors demonstrated that, although wild-type tumors displayed normal architecture of RMS, *six1b*$^{-/-}$ tumor cells displayed a more elongated morphology with higher cytoplasmic-to-nuclear ratios, reminiscent of skeletal muscle differentiation (Figure 2F). In alignment with the slow growth rate, staining for pH3 in *six1b*$^{-/-}$ ($n = 3$) tumors trended toward lowered intensity compared with prominent pH3-positive staining in wild-type zRMS tumors ($n = 4$). This downward shift did not reach statistical significance ($p = 0.081$), likely because of the small number of *six1b*$^{-/-}$ tumors that formed and were evaluable. Nevertheless, the reduction in GFP+ tumor growth in *six1b*$^{-/-}$ zebrafish indicates that *six1b* plays a critical role in zRMS progression, at least in part by controlling RMS cell proliferation, but we cannot rule out the potential of non-cell-autonomous effects from the *six1b*-deficient microenvironment in this model.

SIX1 KD inhibits human RMS growth and progression

The tumors that formed in *six1b*$^{-/-}$ zebrafish displayed an elongated, more spindle-cell-like morphology, suggesting that the RMS cell state fundamentally differs between RMS cells derived from wild-type and *six1b*-depleted animals. To identify whether similar changes occur in human RMS, we examined the morphology of SMS-CTR and RD cells that were transduced with SIX1 short hairpin RNAs (shRNAs). Within approximately five passages after stable SIX1 knockdown (KD), both RMS cell lines exhibited a significantly altered, elongated morphology, distinguishing them from control cells (Figures 3A and 3B).

To determine whether SIX1 KD impairs tumor growth in a cellautonomous manner, we next assessed the *in vivo* outcomes of SIX1 KD in RMS using a mouse xenograft model. SMS-CTR Scramble and SIX1 KD cells were xenografted subcutaneously into the flanks of immunocompromised *NOD/SCID/IL2Rγ* mice and screened weekly for tumor growth. Tumor growth over time, as represented by tumor volume and final tumor weight, was reduced significantly /almost halted in SIX1 KD tumors compared with Scramble tumors (Figures 3C–3E). Histological characterization of the dissected control and SIX1 KD tumors by H&E revealed clear histological distinctions between Scramble and SIX1 KD tumors; all Scramble tumors exhibited high cell density, whereas SIX1 KD tumors were sparsely populated with cells distinguished by elongated nuclear and cytoplasmic morphology (Figure 3F). Notably, upon staining xenografted tumors for pH3, we found that SIX1 KD tumors exhibited significantly less mitotic activity than Scramble tumors (Figure 3G), but apoptosis, as measured by cleaved caspase-3 (CC3) staining, was unchanged (Figure S3). These data demonstrate that the profound differences in *in vivo* tumor growth between Scramble and SIX1 KD RMS tumors can be largely attributed to the lower proliferative capacity of SIX1 KD tumors and are not due to higher levels of apoptosis.

SIX1 KD induces myogenic differentiation in RMS cells

Loss of SIX1 suppresses *in vitro* and *in vivo* RMS growth and leads to alterations in cell morphology, consistent with morphological changes that occur during myogenic differentiation. Because SIX1 KD induced profound cell elongation and anti-proliferative phenotypes in our RMS cell lines, we wanted to determine whether these phenotypes were a consequence of SIX1 directly regulating a pro-proliferative transcriptional program or a secondary consequence of another upstream program regulated by SIX1. We hypothesized that SIX1 overexpression in RMS may regulate an early myogenic transcriptional program that supports RMS cell proliferation and self-renewal (Laclef et al., 2003; Relaix et al., 2013). Therefore, to delineate the transcriptional program coordinated by SIX1 in RMS, we performed RNA-seq on our SMS-CTR Scramble and SIX1 KD cell lines.

The RNA-seq analysis revealed a total of 853 differentially expressed genes (|fold change/ ≥ 1.5, false discovery rate [FDR] ≤ 0.25) between SMS-CTR Scramble and SIX1 KD cells (Figure 4A). Muscle specification genes such MYOG, MYMK, and MYMX were marked as significantly upregulated, whereas genes known to regulate cell motility and invasion, such as TWIST2 and L1CAM, were significantly downregulated (Figure 4A; Altevogt et al., 2016; Katoh and Katoh, 2008; Lo et al., 2007). To further identify dysregulated pathways upon SIX1 KD, we performed a gene set enrichment analysis (GSEA) (Subramanian et al., 2005), which revealed positive enrichment of muscle cell differentiation and contractile muscle gene signatures in SIX1 KD cells (Figure 4B) and negative enrichment of chromatin assembly and developmental cell growth signatures (Figures 4B and S4A). Upon closer inspection of gene expression within the Molecular Signatures DataBase (MSigDB) myogenesis hallmark pathway, we again observed a clear switch in the expression pattern of canonical myogenic genes from low expression in Scramble cells to higher expression in SIX1 KD cells (Figure 4C).

To validate expression changes observed in SIX1 KD cells by RNA-seq, we performed qRT-PCR in SMS-CTR and RD cell lines for a subset of differentially expressed myogenic genes identified from our RNA-seq analysis. Compared with their respective Scramble control cells, SMS-CTR and RD SIX1 KD cells expressed reduced levels of *PAX7* (a TF enriched in muscle progenitors) and expressed higher levels of the MRFs *MYOD1, MYOG*, and *MYF6*. In agreement with our RNA-seq results, we also observed increased expression of genes required for myoblast fusion: *MYMK* and *MYMX* (Figure 4D; Leikina et al., 2018). To further examine whether SIX1 KD cells underwent myogenic differentiation, we stained SMS-CTR and RD SIX1 KD cells for myosin heavy chain (myHC), a marker of terminal muscle differentiation. In both cell line models, SIX1 KD cells exhibited higher proportions of myHC+ cells (Figures 4E and 4F) and were more frequently multinucleated than Scramble cells (Figure 4G). These data indicate that SIX1 KD RMS cells are more capable of progressing toward differentiated and multinucleated myofibers, in contrast to control cells, which maintain their muscle progenitor state.

To determine whether this muscle differentiation phenotype observed with SIX1 loss in human RMS models is conserved in the zRMS model, we additionally stained wild-type and *six1b*$^{-/-}$ zRMS tumors for Pax7 and myHC. In evaluable wild-type and *six1b*$^{-/-}$ tumor sections, we observed a decrease in Pax7 staining in *six1b*$^{-/-}$ tumors compared with

wild-type tumors (Figure S5A), indicative of a shift in differentiation status of the tumors toward a more myotube-like state. In one particular *six1b*$^{-/-}$ tumor, we observed strong myHC staining in the tumor section, which contrasted the largely absent myHC staining in all wild-type tumor sections (Figure S5B). These data demonstrate that *SIX1* represses a myogenic differentiation program in RMS cells in human and zebrafish models.

SIX1 globally regulates stem/oncogenic and myogenic differentiation genes through fine-tuning of superenhancer activity

To decipher the mechanism by which SIX1 loss in RMS cells results in activation of myogenic differentiation genes, we performed an initial TF motif analysis using the RCisTarget R package to identify direct transcriptional regulators of our differentially expressed genes (Figure S6A). Intriguingly, we observed that 41% (350 of 853) of differentially expressed genes upon SIX1 KD were predicted to be regulated by the E box myogenic TFs *MYOD1* and/or *MYOG*, but only 4% (37 of 853) of these genes were predicted to be directly regulated by SIX1 (Figure S6B). Thus, we hypothesized that SIX1 loss must induce muscle differentiation of RMS cells via reprogramming of myogenic TFs.

To determine how loss of the SIX1 TF activates a myogenic differentiation program, we performed chromatin immunoprecipitation sequencing (ChIP-seq) using a polyclonal antibody against SIX1. We also performed ChIP-seq against the master regulator of the myogenic lineage, MYOD1, and the active enhancer/chromatin histone mark H3 lysine 27 acetylation (H3K27ac) in SMS-CTR Scramble and SIX1 KD cell lines. Reflecting levels of shRNA-mediated SIX1 KD, we observed reduced genome-wide binding of SIX1 in both SIX1 KD lines compared with Scramble cells (Figure 5A), and sites of reduced SIX1 binding were highly enriched for SIX1/2 consensus motifs (Figure 5B). We further annotated genetic loci exhibiting at least 1.5-fold reduced SIX1 binding in both SIX1 KD lines compared with the control and found that SIX1 binding was reduced at gene loci involved in stem cell differentiation, Ras signaling, and cytoskeletal organization (Figure 5C). At sites of 1.5-fold reduced SIX1 binding, we additionally observed decreases in H3K27ac signal and in MYOD1 binding (Figure 5D). The alterations in MYOD1 binding did not appear to be dependent on an interaction with SIX1 or on the levels of MYOD1 because no consistent interaction was detected between the two proteins, and the protein levels of MYOD1, despite an increase in mRNA levels (Figure 4D), were only mildly reduced in the presence of SIX1 KD (Figures S7B and S7C). Given the alterations to H3K27ac observed with SIX1 KD, our data suggest that SIX1 regulates large-scale transcriptional programs through mechanisms beyond direct transcriptional induction of in *cis* genes.

To examine whether SIX1 levels influence enhancer activity, we compared enhancers and superenhancers (SEs) via ranked H3K27ac signal between Scramble and SIX1 KD cells. Overall, 4.14%, 5.24%, and 7.37% of total H3K27ac peaks in Scramble (1,470), SIX1 KD5 (1,452), and SIX1 KD6 (1,322) cells, respectively, corresponded to SEs, which are characterized by long-ranging (over 12.5 kb) clusters of strong H3K27ac signal (Lovén et al., 2013; Whyte et al., 2013). Of note, we found that many oncogenic and myogenic genes marked as differentially expressed upon SIX1 KD in our RNA-seq dataset were

associated with SEs. For example, in SIX1 KD cells, we observed a down-ward shift in ranked H3K27ac signal at the SE associated with the Notch effector and muscle stem cell-enriched gene *HEYL* (Noguchi et al., 2019) from 669 in Scramble cells to 1,130 and 1,804 in SIX1 KD5 and KD6 cells, respectively . We also observed an upward shift of H3K27ac signal at the SE associated with the contractile muscle genes *TNNT2* and *TNNI1*, denoted as the *TNNT2* SE by the rank ordering of SEs (ROSE) algorithm from rank 342 in the control condition to 178 and 150 under the SIX1 KD conditions (Figure 5E). We further annotated Scramble and SIX1 KD SEs by closest genes and discovered that, although strong SE activity occurred at myogenic programs under both conditions, SEs in SIX1 KD cells were associated with contractile and striated skeletal muscle, whereas those in the Scramble cell line were associated with commitment to the skeletal muscle lineage and earlier-stage muscle pathways (Figure 5F). These results suggest that SIX1 KD impairs enhancer activity and myogenic TF binding at early muscle or myoblast identity transcriptional programs. In agreement with this finding, we observed reduced SIX1 binding and H3K27ac signal paired with markedly less MYOD1 binding at the *LGR5* enhancer and *HEYL* SE, two known regulators of muscle stem cell fate decisions (Leung et al., 2020; Noguchi et al., 2019; Figure 5G). Notably, we observed loss of MYOD1 binding and H3K27ac/SIX1 signal at the *SIX1* SE in SIX1 KD cells, which reveals a positive feedback circuit inducing SIX1 expression in RMS that is antagonized by inhibition of SIX1 and subsequent loss of MYOD1 at its SE element (Figure 5G). Additional SE elements within known stem cell maintenance genes showed reduced binding in SIX1 KD cells, and this reduced binding was associated with weakened SE activity and reduced mRNA expression (Figures 5H and S7D). These data suggest that loss of SIX1 results in decreased open chromatin (as measured by H3K27ac) at enhancers/SEs associated with self-renewal and oncogenic genes, resulting in reduced MYOD1 binding and subsequent downregulation of stem and oncogenic genes.

SIX1 loss alters MYOD1 occupancy at muscle differentiation and stem/oncogenic loci

By regulating SE activity, we reasoned that downstream accessibility of myogenic TFs at stem/oncogenic and myogenic regulatory elements could be affected by SIX1 KD. Although we noted a slight reduction in overall MYOD1 protein levels in our stable SIX1 KD lines (Figure S7B), the degree of MYOD1 downregulation under the KD condition (approximately 20%) was not concordant with the degree of reduced MYOD1 binding at the same SE sites where SIX1 was heavily bound (approximately 40%) (Figure 5D). Intriguingly, we observed that SIX1 KD resulted in a shift in MYOD1 distribution from distal intergenic/enhancer to promoter regions (Figures 6A and 6C), suggesting that accessibility of binding to enhancers, which is reduced by SIX1 KD, may be a major mechanism for redistribution of MYOD1 away from enhancers and to promoters. Moreover, nearest gene annotation of MYOD1 peaks showed that MYOD1 bound at distal intergenic regions was associated with non-muscle cell fate commitment pathways, whereas MYOD1 bound at promoter regions was associated with skeletal muscle development and cell cycle progression pathways (Figure 6D). To assess whether SIX1 KD could redirect gene programs of other myogenic TFs, we additionally performed cleavage under targets and release using nuclease (CUT&RUN) (Skene and Henik-off, 2017) for MYOG and observed differential MYOG binding between Scramble and SIX1 KD cells at regulatory elements of genes associated with myotube differentiation and the G2/M cell cycle checkpoint, two

pathways where we observed enrichment for MYOD1 promoter binding in SIX1 KD cells (Figures 6D and S8B). Thus, reinstatement of MYOD1 as a myogenic differentiation factor in SIX1 KD cells can be explained in part by a preferential shift of MYOD1 binding from distal stem/oncogenic SEs, where SIX1 is highly bound, to the promoters of muscle differentiation genes and an increase in binding of MYOG at muscle differentiation gene promoters. In line with the observation that residual MYOD1 protein in SIX1 KD cells is retained preferentially at loci promoting differentiation, whereas we observed dramatic loss of MYOD1 binding at the *HEYL* and *SIX1* SEs (Figure 5G), we saw improved MYOD1 binding and enhanced MYOG and MYOD1 binding at the myogenic *MYMK* and *MYLK2* loci (Leikina et al., 2018; Shi et al., 2017; Figure 6E). To validate the shift in MYOD1 occupancy at differentiation and progenitor-related genes in SMS-CTR and RD cells, we performed MYOD1 CUT&RUN followed by qPCR (C&R qPCR), which we used as an orthogonal method to ChIP to detect MYOD1 protein binding to DNA using far fewer cells in our slow-growing RD SIX1 KD5 cells. We found that, in SIX1 KD SMS-CTR cells as well as SIX1 KD RD cells, MYOD1 was bound more abundantly at loci associated with differentiation genes as opposed to myoblast or oncogenic genes (Figure 6F). These results reflect similar observations of MYOD1 genomic occupancy shifting as a consequence of myoblast formation or RMS induction toward differentiation (Cao et al., 2010; Li et al., 2019; MacQuarrie et al., 2013; Pomella et al., 2021; Soleimani et al., 2012). Our data demonstrate that SIX1 regulates a large-scale proliferative and less differentiated cell identity program in RMS by maintaining MYOD1 binding at enhancers and SEs, resulting in a loss of promoter-driven myogenic gene transcription. Thus, SIX1 loss leads to an altered myogenic TF DNA binding landscape that is more permissive for expression of contractile muscle genes over expression of stem-related genes regulated by SEs.

SIX1 expression is inversely correlated with a myotube gene signature in individuals with RMS

The profound myogenic transcriptional program induced upon SIX1 inhibition suggests that overexpression of SIX1 may serve as an upstream orchestrator of the aberrant muscle differentiation observed in RMS, as it does in normal muscle development (Grifone et al., 2004). To test this hypothesis, we examined whether SIX1 expression in samples from individuals with RMS correlates with an early myogenic transcriptional landscape. Using a recently published human pluripotent stem cell (hPSC) dataset (Choi et al., 2020) aimed at defining the transcriptional landscape at multiple stages of human myogenic differentiation, we derived a myogenic differentiation signature from PAX7+ skeletal muscle progenitors and their final states as multinucleated myotubes. With these hPSC data to serve as case-controls for differentiated muscle and muscle progenitors, respectively, we applied a signature scoring method (*S* score) described by Hsiao et al. (2013) to quantitatively score test data, RMS RNA-seq samples, regarding their concordance with the gene expression signatures derived from empirical myotube progenitor data (Figure 7A). To test the performance of our *S* score methodology, we confirmed, using the case-control hPSC data, that *S* scoring could segregate PAX7+ progenitors, MYOG+ myoblasts, and differentiated myotubes in a stepwise manner, where MYOG+ cells displayed an intermediate *S* score between muscle progenitors and myotubes (Figure 7B). Furthermore, we calculated an *S* score for our SIX1 KD RNA-seq samples based on the myotube signature and were able

to distinguish Scramble from SIX1 KD RMS cells based on this scoring method. SIX1 KD cells demonstrated greater alignment with the myotube signature, consistent with the results of other enrichment scoring methods (Figures 4 and 7C). Importantly, using this quantitative scoring technique, we can assess in which stage of the myogenic differentiation cascade our RMS cells lie.

We next assessed how SIX1 expression correlates with myotube *S* scores in samples from individuals with RMS. In the St. Jude iRDb cohort, we found a modest and statistically significant inverse correlation between SIX1 expression and myotube *S* scores (Figure 7D; Spearman correlation, $R = -0.36$; $p = 0.0012$). We additionally applied the same signature scoring algorithm to generate a SIX1 KD signature using our SIX1 KD RNA-seq dataset as case (KD)-controls (Scramble) and *S* scored St. Jude and GEO: GSE108022 RMS samples based on SIX1 KD and myotube gene signatures. We observed strong positive correlations (St. Jude: $R = 0.57$, $p < 0.001$; GEO: GSE108022: $R = 0.61$, $p < 0.001$) between the two signatures in individuals with RMS, indicating that loss of SIX1 expression in RMS cells induces a transcriptional program similar to one observed when a myoblast transitions to the myotube fate (Figure 7E).

Given the concordance of the SIX1 KD signature with the myotube signature, we next sought to examine whether these two signatures could be used to distinguish advanced RMS disease from primary disease. Of the 71 samples with complete RNA-seq data available from the St. Jude iRDb cohort, three of these individuals had RNA-seq performed at multiple stages of the disease. Filtering down our analysis to these three individuals, we examined whether disease recurrence was associated with changes in myogenic differentiation state. By myotube and SIX1 KD *S* scoring, we observed that tumor expression profiles at diagnosis and disease recurrence states were distinguishable by differentiation and SIX1 KD scores, where relapsed tumors exhibited lower SIX1KD and myotube *S* scores than their tumor at diagnosis (Figure 7F). Of note, we observed that the two relapsed tumor samples from individual B012 had lower myotube and SIX1 KD *S* scores compared with the tumor at diagnosis (Figure 7F). In summary, the transcriptional program controlled by SIX1 in RMS is intimately linked to myogenic differentiation status, which is a driving force of RMS progression.

DISCUSSION

Repression of myogenic differentiation programs is a known critical attribute of RMS, where dysfunctional MYOD1 and MYOG activity is thought to drive the disease (Hayes et al., 2018; Liu et al., 2020; MacQuarrie et al., 2013; Phelps et al., 2016; Tenente et al., 2017). An unresolved question that persists in the field of RMS is why RMS tumors express the myogenic TFs MYOD1 and MYOG but fail to progress past the apparent myoblast progenitor state (An et al., 2017; Rudnicki et al., 1993; Weintraub et al., 1989). Although it is known that MYOD1 and MYOG have distinct subprograms that can drive self-renewal or skeletal muscle differentiation, departure of these MRFs from their canonical ability to execute the complete sequence of skeletal muscle development in RMS invokes other factors that may repress the ability of MYOD1 to act on its differentiation programs. Therefore, identification of other regulatory proteins that alter the context-specific functions of MYOD1

has become a core area of RMS studies (Londhe and Davie, 2011; MacQuarrie et al., 2013; Yang et al., 2009). In this study, we report that the SIX1 homeobox TF acts upstream of the MYOD1 and MYOG TFs in FN RMS, maintaining arrest of RMS cells in a self-renewing muscle progenitor state through a mechanism distinct from that in embryonic myogenesis. In the developmental context, the *SIX1* homeobox gene is highly expressed in early muscle development and is responsible for direct activation of MRF expression, ultimately leading to muscle differentiation (Berti et al., 2015; O'Brien et al., 2014). In RMS, however, we observe that SIX1 engages MYOD1 at stem and oncogenic SEs instead of gene promoters responsible for muscle differentiation and prevents MYOD1 from transcriptionally steering RMS cells toward the expected myotube fate. In our zebrafish and human FN RMS models, we demonstrate that genetic inhibition of *six1b/SIX1* can trigger activation of a muscle differentiation gene program in RMS cells, halting their growth and spread. This phenotype, increased differentiation, contrasts the net effect of SIX1 loss during myogenesis, where SIX1 (and SIX1/SIX4) deficiency results in a decrease in differentiated myofibers (Laclef et al., 2003; Relaix et al., 2013; Wu et al., 2014). We propose that the phenotypic difference arises because SIX1 plays dual roles in myogenesis, promoting differentiation (Grifone et al., 2004; Liu et al., 2013; Niro et al., 2010; Wu et al., 2013; Yajima et al., 2010) and muscle precursor proliferation (Grand et al., 2012; Grifone et al., 2005; Nord et al., 2013; Talbot et al., 2019), whereas in RMS, we find that SIX1 exclusively promotes proliferation. These two modes of function may be driven by differences in SIX1 expression. SIX1 expression is highest during the early steps of myogenesis, promoting muscle precursor proliferation; however, SIX1 is downregulated during the final stages of embryonic myogenesis, when it promotes muscle fiber differentiation (Berti et al., 2015; Choi et al., 2020; O'Brien et al., 2014). Therefore, RMS may capture the developmental window of myogenesis where SIX1 is at peak expression. Further work is needed to clarify whether the pro-stem-cell function of SIX1 in myogenesis exactly mirrors its role in RMS or whether SIX1's function in RMS is, instead, *de novo*.

In most studies implicating *SIX1* in cancer progression, SIX1 ostensibly acts as a TF that induces expression of downstream tumor-promoting genes. Notably, the pro-metastatic functions of *Six1* in RMS have been reported to be channeled through one of Six1's transcriptional targets, *EZR*, a cytoskeletal protein (Yu et al., 2004, 2006). In this study, we show for the first time that SIX1 promotes tumor growth/progression via alteration of global transcriptional programs of muscle cell identity. Thus, although direct targets such as *EZR* likely contribute to its aggressive functions in RMS, the major function of SIX1 in RMS progression appears to be through changing cell fate by regulating transcriptional programs upstream of myogenic TFs. In normal development, *Six1* loss in muscle precursor cells leads to reduced MRF expression and concomitant defects in skeletal muscle formation (Bessarab et al., 2008; Grand et al., 2012; Grifone et al., 2004; Laclef et al., 2003; Relaix et al., 2013; Santolini et al., 2016). In the context of FN RMS, we observe that SIX1 KD is associated with loss of progenitor gene expression but gain of a muscle differentiation gene expression program, raising the question of how SIX1 activates a differentiation program while it is itself suppressed. By ChIP-seq, we observe that genome-wide SIX1 binding closely overlaps with H3K27ac marks at promoters and SE regulatory elements. SIX1 KD leads to decreases in SIX1 binding at cytoskeletal, cell division, and stem-related loci, which

aligns with previously characterized roles of SIX1 (Coletta et al., 2004; Kingsbury et al., 2019; Lee et al., 2018; McCoy et al., 2009; Yu et al., 2004, 2006). On a global scale, SIX1 binding is enriched at SEs, enhancers, and promoters associated with cell division, cell identity, and muscle specification. Upon SIX1 KD, SE activity, as approximated by the H3K27ac signal, is diverted from progenitor/stemrelated SEs to SEs associated with that of forming contractile muscle and other structural components of skeletal muscle differentiation, which manifests as the multinucleated and elongated morphology of SIX1 KD cells. In addition to these direct forms of transcriptional regulation at target loci or at distal regulatory elements, we found that SIX1 can indirectly influence the DNA binding activity of MYOD1 and possibly other myogenic TFs by modifying the landscape of active chromatin and, consequently, TF binding accessibility at differentiation loci.

Pluripotency and cell type determination are controlled by the occupancy of master TFs and cell-type-specific TFs at enhancer regions governing cell fate decisions (Heinz et al., 2015; Whyte et al., 2013). Within the repertoire of muscle-lineage enhancers, several TFs, which, based on our studies, include *SIX1*, have come to light as master TFs that initialize the myogenic lineage by sitting poised at myoblast enhancer elements and then become overactive in the context of RMS (Li et al., 2019; Liu et al., 2020; Phelps et al., 2016; Pomella et al., 2021). Notably, these factors include the developmental TFs *SNAI1/2* and *TWIST2*, which, similar to *SIX1*, are found at stem and myogenic enhancer elements in RMS and are drivers of epithelial-to-mesenchymal transition (EMT), cell migration, and tissue repair (Li et al., 2019; Pomella et al., 2021; Soleimani et al., 2012). Our focused study of *SIX1* compounds growing evidence showing that the composition of TFs at muscle-specific enhancers controls the differentiation state of RMS cells, which raises multiple questions. First, which factors cause SIX1 to become overexpressed in FN RMS, particularly given the absence of *SIX1* amplification or any common perturbation of the locus? Although *SIX1* has been identified as a target down-stream of the *PAX3-FOXO1* fusion, the mechanism leading to SIX1 overexpression in FN RMS is less understood (Khan et al., 1999). Second, our findings raise the question of how diverse driver mutations associated with FN RMS impinge on myogenic epigenetic/transcriptional programs in a fashion similar to the *PAX3-FOXO1* fusion protein in FP RMS (Gryder et al., 2017, 2019, 2020). Notably, genome-wide PAX3-FOXO1 fusion binding establishes SEs at myogenic genes and recruits the co-activator proteins p300, BRD4, and Mediator (Gryder et al., 2017), and similar functions may apply to TFs like *SIX1* in FN RMS. Finally, these studies raise the question of whether RMS cells can be irreversibly reprogrammed to follow the proper cascade of myogenic differentiation through targeting master TF activity. Although there are still many barriers facing the viability of TFs as pharmacological targets, dissection of mechanisms that modulate specific TF activities can potentially reveal druggable nodes that control cell-type-specific transcriptional programs. For example, the requirement of an Eyes Absent (EYA) phosphatase co-factor interaction with SIX1 to strongly activate downstream target transcription represents one targetable node for SIX1 activity our group is actively interrogating (Farabaugh et al., 2012; Li et al., 2003; Patrick et al., 2013; Zhou et al., 2020). Thus, it will be of future interest to determine whether the EYA phosphatase plays a similar role together with SIX1 in trapping RMS cells in a progenitor-like state.

Our study demonstrates that SIX1 prevents FN RMS from differentiating via regulating transcriptional output at stem versus myogenic genes. We show that FN RMS differentiates into non-proliferative myotube-like cells following SIX1 inhibition and that the differentiation program is achieved by a shift in MYOD1 binding and enhanced transcriptional activity from genetic loci that foster cell growth to loci that specify and drive the myogenic lineage. These findings define an epigenetic function of SIX1 in balancing the growth and differentiation properties intrinsic to the myogenic lineage and suggest that inhibition of SIX1 may be of therapeutic value in RMS.

Limitations of the study

In this study, although it is clear that epigenetic changes occur from specific loss of SIX1, the antibody used for ChIP-seq and C&R, although against SIX1, may cross-react with other related SIX TFs (Qamar et al., 2012). It should also be noted that there are several TFs in addition to SIX1 reported to control the RMS differentiation state (Li et al., 2019; Liu et al., 2020; Pomella et al., 2021). Future work should seek to investigate the kinetics and composition of nuclear factors occupying myoblast and myotube genes; such complexes could potentially be leveraged to bias MYOD1 activity to differentiation loci instead of proliferative myoblast loci in advanced RMS.

STAR★METHODS

RESOURCE AVAILABILITY

Lead contact—Further information and requests for resources and reagents should be directed to and will be fulfilled by the lead contact, Heide L. Ford (heide.ford@cuanschutz.edu).

Materials availability—This study did not generate new reagents.

Data and code availability

- Raw NGS datasets (RNAseq, ChIPseq) generated in this paper are deposited on GEO and will be available at publication date. Accession numbers of our NGS data and publicly available clinical datasets are listed in the key resources table.
- Original code for S-scoring calculations can be found on GitHub(https://github.com/jywhsu/weighted-genesig-scoring).
- Additional information required to analyze the data reported in this paper are available from the lead contact upon request.

EXPERIMENTAL MODELS AND SUBJECT DETAILS

Clinical RNAseq datamining—Clinical sarcoma expression data was obtained from the NCI Oncogenomics database managed by Dr. Javed Khan at the NIH. Clinical RMS RNAseq expression data was accessed and downloaded from the St. Jude PeCAN Cloud portal and Integrated Rhabdomyosarcoma Database.

Zebrafish maintenance—Zebrafish lines used in this study were maintained in compliance with the University of Colorado Anschutz Medical Campus IACUC guidelines and policies. The *six1b*^{oz1} mutant line used in this study was a generous gift from Dr. Sharon Amacher's lab and crossed as heterozygotes to generate wildtype, heterozygote, and mutant homozygote progeny. Fish finclips were genotyped (Talbot et al., 2019) using the primers Forward: ATTCCGCTTCCTTCGTAGCATC, and Reverse: TGCAGCTTCGGGTGATTGTG, followed by a 2hr MwoI digest at 60°C. Developmental stages used for zebrafish whole-mount *in-situ* hybridization experiments are indicated in the figure. Zebrafish tissue used for Western blot experiments, sectional ISH, and qRT-PCR captured adult stages between 3 and 6 months post fertilization.

Zebrafish ERMS studies—Zebrafish ERMS tumors were established using previously described methods by the Langenau Lab (Langenau et al., 2007). Briefly, *rag2-kRASG12D* and *rag2-eGFP* plasmids were linearized with NotI and purified using the Zymo Clean and Concentrator kit. Linearized DNA was diluted to a stock concentration of 100 ng/μL and injected with phenol red dye into the single-cell stage of embryos for a final concentration of 5pg/embryo per *rag2* plasmid. Zebrafish tumor initiation events were recorded at 36 days post-injection and every week thereafter until 180 days. Tumor area was measured weekly using a Leica epifluorescent stereomicroscope along with body length to adjust for changes in basal growth of fish.

Cell culture and cell lines—FP-RMS and FN-RMS cell lines used in this study were a generous donation from Dr. Mark Hatley. Cell lines manipulated in this study (SMS-CTR and RD) were maintained at 37°C and 5% CO_2 in Dulbecco's Modified Eagle Medium (DMEM) supplemented with 10% FBS and 1% penicillin/streptomycin. Cell lines were tested for mycoplasma (Lonza MycoAlert) at least twice per year and only mycoplasma-negative cell lines were used in this study. All cell lines were STR authenticated by the University of Colorado Cancer Center Tissue Culture shared resource.

Mouse studies—All mouse studies were performed in 6–8 week old immunodeficient NOD/SCIDg (NSG) of mixed genders. For mouse xenograft experiments, 2×10^5 cells suspended in a 200μL 1:1 matrigel:1X PBS suspension were subcutaneously injected into either the left or right flank of the mouse, with each mouse receiving a Scramble and SIX1 KD injection on either the left or right flank. Tumor growth was measured weekly for 12 weeks using calipers or until tumors surpassed a tumor volume of 1000 mm^3 (1 cm^3). All animal studies were performed according to protocols approved by the University of Colorado Institutional Animal Care and Use Committee.

METHOD DETAILS

***In-situ* hybridization on zRMS sections—**3–6 month old zebrafish tumor and normal muscle control tissues were fixed in 4% PFA for 2 h at room temperature (RT), rinsed with PBS, and embedded in 1.5% agar/5% sucrose solution. Agar-sucrose tissue blocks were flash-frozen in liquid nitrogen and subsequently cryosectioned on a microtome. Frozen sections were defrosted for 1 h at RT then incubated overnight at 70°C in six1b probe (provided by Vladimir Korzh, Institute of Medical and Cellular Biology, A*STAR, Proteos,

Singapore) diluted 1 μg/mL in hybridization buffer (1X SSC buffer, 50% formamide, 10% dextran sulfate, 1 mg/mL yeast tRNA, 1X Denhardt's). Sections were then washed 3 ×30 min at 70°C (Wash: 1X Saline Sodium Citrate [SSC] buffer, 50% formamide, 0.1% Tween 20) followed by 3 × 10 min at RT in MABT (1X maleic acid buffer, 20% Tween 20), and incubated 2 h in blocking solution (MABT, 20% sheep serum, 10% Boehringer Blocking Reagent). Sections were then incubated overnight at RT in 1:2000 anti-digoxigenin antibody diluted in blocking solution, washed 4 × 20 min at RT in MABT, then 2 × 10 min wash in AP staining buffer (100 mM NaCl, 50 mM MgCl2, 100 mM Tris pH9.5, 0.1% Tween 20), and stained overnight at 37°C in 3.5μL/mL nitro-blue tetrazolium (NBT), 2.6μL/mL 5-bromo-4-chloro-3′-indolyphosphate (BCIP), 10% polyvinyl alcohol in AP staining buffer. Slides were rinsed 2X in PBS+0.1% Tween 20, 2X in ddH2O, dehydrated through ethanol solutions, cleared in xylene and coverslipped in Permount.

Whole-mount zebrafish embryo *in situ* hybridization—Whole-mount RNA *in situ* hybridization (ISH) in zebrafish embryos was performed as previously described (Thisse et al., 2004). DIG-conjugated antisense probes (gifts from Simon Hughes' lab) were T7 or T3 transcribed for *pax3a*, *myod1*, and *myogenin* from pCS2+ backbone plasmids. *Post-hoc* genotyping of ISH-stained embryos was performed by incubating single embryos in 300 mM NaCl overnight at 65°C to reverse crosslinks. DNA was purified from each embryo by phenol-chloroform extraction and genotyped as described previously (Talbot et al., 2019).

Lentiviral cell line transduction—Stable SIX1 KD was achieved in SMS-CTR and RD cell lines by lentiviral transduction of two pLKO.1-derived shRNAs targeting the SIX1 CDS, subsequently denoted throughout the text as SIX1 KD5 and KD6. Control pLKO.1 Scramble cells were also transduced alongside SIX1 KD cells. pLKO.1 shRNA plasmids were transfected into HEK293T cells (293T) along with pMD2G and psPAX2 envelope and packaging plasmids. Viral particles were collected from 293T cells 48-h post-transfection, passed through a 0.45 μm filter syringe, and treated with 6–8 μg of polybrene prior to infecting target cells. 24-h post-viral infection, cells were selected with 2.0 μg/mL (SMS-CTR) or 1.0 μg/mL (RD) puromycin in 10% FBS/DMEM for 1 week and maintained in half the puromycin dose for remaining experiments.

IncuCyte cell growth assay—RMS cell growth was measured on an IncuCyte Zoom (Essen Bioscience) Live-Cell Analysis platform. For cell growth, cells were plated at a concentration of 2500 cells/well in a 96-well plate and imaged every 12 h with a 4X objective. Cell growth was measured by percent confluence and results presented in this study are normalized to percent confluence at time point zero (% Confluence to Baseline).

qRT-PCR—Cells were harvested for RNA using the Zymo Direct-zol RNA isolation kit and cDNA was synthesized using the Bio-rad iScript reverse transcription kit following manufacturer's instructions. Quantitative reverse-transcriptase PCR (qRT-PCR) was performed using Biorad ssoFast Evagreen supermix on a Biorad CFX96 qPCR instrument. SYBR primers used in this study are detailed in Table S1. Zebrafish tissues were snap-frozen in Trizol reagent, allowed to thaw, and homogenized using a plastic pestle. Homogenized tissue was then harvested for RNA using the Zymo Direct-zol kit. cDNA

was synthesized using the ThermoFisher Verso cDNA Synthesis kit and qPCR reactions were performed using Taqman Gene Expression Master mix on an Applied Biosystems StepOnePlus instrument. Taqman probes used in this study are detailed in Table S3.

Western Blotting—Whole cell protein extracts were harvested by lysing cells in RIPA buffer treated with protease inhibitors and further lysed via sonification. 20–50 μg of whole cell lysates were boiled with sample buffer and run through a 10% polyacrylamide gel. After PAGE gel electrophoresis, gels were transferred onto PVDF membranes, blocked in 5% Milk/TBST, and incubated with primary antibodies diluted in 5%BSA/TBST overnight at 4°C. Blots were incubated with HRP-conjugated secondary antibodies raised against primary antibody species at a 1:1000 dilution and chemiluminescence detected with Pierce ECL Western Blotting substrate. Chemiluminescence was imaged using an OdysseyFc imaging instrument. Between all antibody incubations, blots were washed with 1X TBST.

Immunocytochemistry—Cells were plated on 4-well chamber slide and fixed in 4% PFA/PBS for 10 min and permeabilized in 0.1% Triton X-100/PBS (PBST) for 30 min. Chamber slides were next blocked with 15% goat serum/PBST for one hour and incubated in primary antibody solution overnight. The following day, chamber slides were incubated with appropriate fluorophore-conjugated secondary antibodies and mounted with Vectashield mounting medium with DAPI counterstain. All washes between incubation steps were performed with 1X PBS. Mounted slides were imaged on an Olympus BX51 fluorescence microscope. For pH3 and myHC stains, staining was quantified by dividing the number of positively stained cells by the total number of nuclei per field of view. Multinucleated events or fusion indices were quantified by counting the number of nuclei enclosed within a single positively stained myHC unit. For all immunocytochemistry stains, data is represented as image measurements taken over at least three independent experiments with two or more biological replicates per experiment, and two or more fields of view per biological replicate.

Immunohistochemistry—For zRMS studies, tumor-burdened fish were euthanized in ice-water, fixed in 4%PFA overnight at 4°C, washed in PBS for 24 h, decalcified in 20% EDTA pH 8.0 for 24 h, dehydrated in 70% EtOH, and paraffin-embedded. Paraffin-embedded tissues were cut into 10–15 μm thick sections and stained with H&E or further processed for antibody staining. For mouse xenografts following dissection, mouse tumor tissue was fixed in 4% PFA overnight, washed in PBS for 24 h, and dehydrated in 70% EtOH prior to paraffin-embedment. For all downstream IHC stains (zRMS, mouse xenograft, human tissue array), slides were de-paraffinized and retrieved in either pH6 (Six1, myHC) or pH9 (Pax7) Tris/EDTA buffer. Slides were then peroxidase blocked with 3% hydrogen peroxide (in methanol) for 10 min, blocked in serum-free blocking reagent (DAKO) and incubated with primary antibodies for 1hr at room temperature. Appropriate species' secondary antibodies were then incubated for 30 min and developed with DAB stain for 10 min and counterstained with hematoxylin for another 8 min.

RNAseq—Total RNA was isolated from SMS-CTR cells using the Zymo Direct-zol RNA Miniprep Kit and RNA integrity confirmed using TapeStation analysis. Scramble and SIX1

KD SMS-CTR RNA samples were submitted as biological triplicates save for SIX1 KD6, which was submitted as biological duplicates on account of its marked proliferative defects. 100 ng of total RNA per sample was used to construct PolyA-selected RNA libraries for RNAseq and sequenced using paired end reads with 150 cycles on an Illumina NovaSEQ 6000 instrument.

ChIPseq—Human cells along with spike-in Drosophila S2 cells at a 1:10 ratio with human cells were fixed in 1% formaldehyde diluted in growth media for an incubation time of 15 min. Crosslinking was quenched with the direct addition of 1 M Tris pH 7.5 and shaking for 15 min. Cells were gently scraped off plates, pelleted by centrifugation, washed in cold PBS and centrifuged again. Cell pellets were snap frozen in liquid nitrogen and nuclei were extracted from cell pellets. Chromatin was fragmented in sonication buffer (50 mM HEPES pH 7.5, 140 mM NaCl, 1 mM EDTA, 1 mM EGTA, 1% Triton X-, 0.1% Sodium deoxycholate, 0.1% SDS) supplemented with protease inhibitor cocktail using a Branson digital sonifier instrument at 4°C with the following settings: 7 cycles of 30 s ON and 1 m OFF sonification at 50% intensity. Chromatin lysates were incubated with 10 μg antibody-bound Dynabeads overnight and washed in buffers of increasing stringency: 2X sonication buffer, 1X high salt sonication buffer (sonication buffer with 500 mM NaCl), 1X LiCl buffer (20 mM Tris pH 8.0, 1 mM EDTA, 250 mM LiCl, 0.5% NP-40, 0.5% sodium deoxycholate), and 1X TE pH 8.0. Immunocomplexes were eluted in 1% SDS/TE buffer and transferred to Lobind DNA tubes at 65°C for 30 min and crosslinks were reversed over-night by incubating samples at 65°C. RNA and protein were digested by the addition of RNase and Proteinase K, and DNA fragments were purified using phenol-chloroform. ChIPseq libraries were assembled using the KAPA HyperPrep ChIP library kit following manufacturer's settings and were sequenced on an Illumina Nextseq500 machine.

CUT&RUN

500,000 cells/sample were harvested by scraping and were resuspended and washed twice in wash buffer (20 mM HEPES pH 7.5, 150 mM NaCl, 0.5 mM Spermidine) supplemented with protease inhibitor cocktail. Cells were adsorbed onto activated Concavalin A beads for 10 min and then incubated with antibodies O/N at 4°C. After antibody incubation, unbound antibodies were washed away with cold Digitonin buffer (wash buffer + 0.01% Digitonin) and pAG-MNase was added to each sample to produce chromatin fragments under targets for 10 min at RT. Cells were then cooled to 0°C and incubated with ice-cold 100 mM $CaCl_2$ for 2 h at 4°C. MNase digestion was terminated with the addition of a master mix of STOP buffer (340 mM NaCl, 20 mM EDTA, 4 mM EGTA, 50 μg/mL RNaseA, 50 mg/mL Glycogen) and 0.5 ng/ul *E.coli* spike-in DNA and incubated for 10 min at 37°C. DNA was purified using a column purification kit and used for library assembly. Antibody concentrations: 1:100 for rabbit IgG, 1:50 for MYOD1, 1:50 for SIX1, and 1:50 for MYOG. CUT&RUN libraries were assembled using the NEBNext II Ultra Library Prep kit and dual-index primers following manufacturer protocols. Library size distribution was assessed by TapeStation and libraries were subsequently used for CUT&RUN qPCR; primer sequences are described in Table S2.

QUANTIFICATION AND STATISTICAL ANALYSIS

RNAseq analysis—Read QC was performed using fastqc and reads were trimmed with BBDuk to remove Illumina adapter sequences and the first 12 bases on the 5´ ends. Trimmed fastqc files were aligned to the hg38 human reference genome and aligned counts per gene were quantified using STAR (Dobin et al., 2013). Differential gene analysis was performed using the edgeR package (Robinson et al., 2010). Gene Set Enrichment Analysis (GSEA) was performed under default settings using the clusterProfiler R package gseaplot function (Yu et al., 2012). Normalized counts (CPM) were converted to z-scores prior to plotting and heatmaps were created using the pheatmaps R package (https://CRAN.R-project.org/package=pheatmap).

ChIPseq analysis—The quality of the fastq files was accessed using FastQC (https://www.bioinformatics.babraham.ac.uk/projects/) and MultiQC (Ewels et al., 2016). Illumina adapters and low-quality reads were filtered out using BBDuk (http://jgi.doe.gov/data-and-tools/bb-tools). Bowtie2 (v.2.3.4.3) was used to align the sequencing reads to the hg38 reference human genome and to the dm6 Drosophila reference genome (Langmead and Salzberg, 2012). Samtools (v.1.11) was used to select the mapped reads (samtools view -b - q 30) and sort the bam files (Li et al., 2009). PCR duplicates were removed using Picard MarkDuplicates tool (http://broadinstitute.github.io/picard/). To adjust for variations in ChIP reads throughout the ChIPseq protocol across all samples, we normalized ChIP reads to Drosophila spike-in reads per sample. Briefly, the normalization ratio of each sample was calculated by dividing the total number of mapped reads mapping to the Drosophila genome of each sample by the total number of mapped reads mapping to the Drosophila genome of the sample with the lowest number of reads. Using the normalization ratio, random sub-sampling of the reads was performed using samtools view -hs. Bed-tools genomecov was used to create bedgraph files from the bam files (Quinlan and Hall, 2010). Peaks were called using MACS2 (v2.1.2) with default parameters for narrow peaks (–gsize hs –qvalue 0.01) (Zhang et al., 2008). Average profiles were generated using ngs.plot (Shen et al., 2014) and heatmaps were generated using normalized bigwig files with deepTools (Ramírez et al., 2014). Motif analysis was performed on.bam files using HOMER. ChIP peaks were annotated using the ChIPseeker R package (Yu et al., 2015). Pathway enrichment plots were generated using ChIPseeker followed by ClusterProfiler R packages with gene set sizes restricted to 100 to 250 genes and a q-value cut-off of 0.05. Super-enhancers were identified using the Ranking Ordering of Super-Enhancer (ROSE) algorithm using default parameters (Lovén et al., 2013; Whyte et al., 2013) and hockey stick plots were generated in R. ChIPseq track figures were generated using the Washington University Epigenome Browser (Zhou et al., 2011).

Statistical analysis—Quantification of immunohistochemical images was performed using ImageJ. All cell line experiments were performed in at least three independent experiments with at least two biological replicates. Throughout this manuscript, all numeric p values are printed as is on figures. For most figures, measures of variance and centrality are depicted by mean and standard deviation (SD), unless stated otherwise in figure legends. Statistical tests performed are described in figure legends. Scale bars for all microscopy images are labeled underneath their respective figure.

Supplementary Material

Refer to Web version on PubMed Central for supplementary material.

ACKNOWLEDGMENTS

This work was supported by R21CA201809 (to H.L.F. and K.B.A.), R01CA224867 (to H.L.F.), R01CA183874 (to P.J.), GM117964 (to S.L.A.), NS098780 (to S.L.A.), K08CA245251 (to A.D.D.), an Alex's Lemonade Stand Foundation Innovation Award (to H.L.F.), CU Cancer Center Molecular and Cellular Oncology Pilot Grant P30CA046934 (to H.L.F., K.B.A., and P.J.), and training fellowships T32GM763538 and TL1TR001081 (to J.Y.H.). The reported research was supported by NIH/NCI P30CA021765 (to St. Jude Children's Research Hospital Comprehensive Cancer Center), CureSearch for the Children's Cancer Foundation, the Rally Foundation for Childhood Cancer Research, the American Lebanese Syrian Associated Charities (to A.D.D. and S.N.), a Pelotonia fellowship (to J.C.T.), and a University of Maine startup fund (to J.C.T.). This work used the Cell Technologies, Functional Genomics, Pathology, and Biostatistics and Bioinformatics Shared Resource supported by P30CA046934.

REFERENCES

Aibar S, González-Blas CB, Moerman T, Huynh-Thu VA, Imrichova H, Hulselmans G, Rambow F, Marine J-C, Geurts P, Aerts J, et al. (2017). SCENIC: single-cell regulatory network inference and clustering. Nat. Methods 14, 1083–1086. [PubMed: 28991892]

Altevogt P, Doberstein K, and Fogel M (2016). L1CAM in human cancer. Int. J. Cancer 138, 1565–1576. [PubMed: 26111503]

An Y, Wang G, Diao Y, Long Y, Fu X, Weng M, Zhou L, Sun K, Cheung TH, Ip NY, et al. (2017). A molecular switch regulating cell fate choice between muscle progenitor cells and Brown adipocytes. Dev. Cell 41, 382–391.e5. [PubMed: 28535373]

Berti F, Nogueira JM, Wöhrle S, Sobreira DR, Hawrot K, and Dietrich S (2015). Time course and side-by-side analysis of mesodermal, pre-myogenic, myogenic and differentiated cell markers in the chicken model for skeletal muscle formation. J. Anat 227, 361–382. [PubMed: 26278933]

Bessarab DA, Chong S-W, Srinivas BP, and Korzh V (2008). Six1a is required for the onset of fast muscle differentiation in zebrafish. Dev. Biol 323, 216–228. [PubMed: 18789916]

Cao Y, Yao Z, Sarkar D, Lawrence M, Sanchez GJ, Parker MH, MacQuarrie KL, Davison J, Morgan MT, Ruzzo WL, et al. (2010). Genome-wide MyoD binding in skeletal muscle cells: a potential for Broad cellular reprogramming. Dev. Cell 18, 662–674. [PubMed: 20412780]

Cheyette BNR, Green PJ, Martin K, Garren H, Hartenstein V, and Zipursky SL (1994). The Drosophila sine oculis locus encodes a homeodomain-containing protein required for the development of the entire visual system. Neuron 12, 977–996. [PubMed: 7910468]

Choi IY, Lim H, Cho HJ, Oh Y, Chou BK, Bai H, Cheng L, Kim YJ, Hyun S, Kim H, et al. (2020). Transcriptional landscape of myogenesis from human pluripotent stem cells reveals a key role of TWIST1 in maintenance of skeletal muscle progenitors. Elife 9, 1–27.

Coletta RD, Christensen K, Reichenberger KJ, Lamb J, Micomonaco D, Huang L, Wolf DM, Müller-Tidow C, Golub TR, Kawakami K, et al. (2004). The Six1 homeoprotein stimulates tumorigenesis by reactivation of cyclin A1. Proc. Natl. Acad. Sci. U. S. A 101, 6478–6483. [PubMed: 15123840]

Dharia NV, Kugener G, Guenther LM, Malone CF, Durbin AD, Hong AL, Howard TP, Bandopadhayay P, Wechsler CS, Fung I, et al. (2021). A first-generation pediatric cancer dependency map. Nat. Genet 53, 529–538. [PubMed: 33753930]

Dobin A, Davis CA, Schlesinger F, Drenkow J, Zaleski C, Jha S, Batut P, Chaisson M, and Gingeras TR (2013). STAR: ultrafast universal RNA-seq aligner. Bioinformatics 29, 15–21. [PubMed: 23104886]

Dubois L, Frendo JL, Chanut-Delalande H, Crozatier M, and Vincent A (2016). Genetic dissection of the transcription factor code controlling serial specification of muscle identities in Drosophila. Elife 5, 1–23.

Ewels P, Magnusson M, Lundin S, and Käller M (2016). MultiQC: summarize analysis results for multiple tools and samples in a single report. Bioinformatics 32, 3047–3048. [PubMed: 27312411]

Farabaugh SM, Micalizzi DS, Jedlicka P, and Ford HL (2012). Eya2 is required to mediate the pro-metastatic functions of Six1 via the induction of TGF-β signaling, epithelial-to-mesenchymal transition, and cancer stem cell properties. Oncogene 31, 552–562. [PubMed: 21706047]

Grand FL, Grifone R, Mourikis P, Houbron C, Gigaud C, Pujol J, Maillet M, Pagès G, Rudnicki M, Tajbakhsh S, et al. (2012). Six1 regulates renewal during skeletal muscle regeneration. J. Cell Biol 198, 815–832. [PubMed: 22945933]

Grifone R, Demignon J, Houbron C, Souil E, Niro C, Seller MJ, Hamard G, and Maire P (2005). Six1 and Six4 homeoproteins are required for Pax3 and Mrf expression during myogenesis in the mouse embryo. Development 132, 2235–2249. [PubMed: 15788460]

Grifone R, Laclef C, Spitz F, Lopez S, Demignon J, Guidotti J-E, Kawakami K, Xu P-X, Kelly R, Petrof BJ, et al. (2004). Six1 and Eya1 expression can reprogram adult muscle from the slow-twitch phenotype into the fast-twitch phenotype. Mol. Cell. Biol 24, 6253–6267. [PubMed: 15226428]

Gryder BE, Yohe ME, Chou HC, Zhang X, Marques J, Wachtel M, Schaefer B, Sen N, Song Y, Gualtieri A, et al. (2017). PAX3-FOXO1 establishes myogenic super enhancers and confers BET bromodomain vulnerability. Cancer Discov 7, 884–899. [PubMed: 28446439]

Gryder BE, Pomella S, Sayers C, Wu XS, Song Y, Chiarella AM, Bagchi S, Chou HC, Sinniah RS, Walton A, et al. (2019). Histone hyperacetylation disrupts core gene regulatory architecture in rhabdomyosarcoma. Nat. Genet 51, 1714–1722. [PubMed: 31784732]

Gryder BE, Wachtel M, Chang K, El Demerdash O, Aboreden NG, Mohammed W, Ewert W, Pomella S, Rota R, Wei JS, et al. (2020). Miswired enhancer logic drives a cancer of the muscle lineage. IScience 23, 101103. [PubMed: 32416589]

Hanna JA, Garcia MR, Lardennois A, Leavey PJ, Maglic D, Fagnan A, Go JC, Roach J, Wang YD, Finkelstein D, et al. (2018). PAX3-FOXO1 drives miR-486–5p and represses miR-221 contributing to pathogenesis of alveolar rhabdomyosarcoma. Oncogene 37, 1991–2007. [PubMed: 29367756]

Hayes MN, McCarthy K, Jin A, Oliveira ML, Iyer S, Garcia SP, Sindiri S, Gryder B, Motala Z, Nielsen GP, et al. (2018). Vangl2/RhoA signaling pathway regulates stem cell self-renewal programs and growth in rhabdomyosarcoma. Cell Stem Cell 22, 414–427.e6. [PubMed: 29499154]

Heinz S, Benner C, Spann N, Bertolino E, Lin YC, Laslo P, Cheng JX, Murre C, Singh H, and Glass CK (2010). Simple combinations of lineage-determining transcription factors prime cis-regulatory elements required for macrophage and B cell identities. Mol. Cell 38, 576–589. [PubMed: 20513432]

Heinz S, Romanoski CE, Benner C, and Glass CK (2015). The selection and function of cell type-specific enhancers. Nat. Rev. Mol. Cell Biol 16, 144–154. [PubMed: 25650801]

Hinson ARP, Jones R, Crose LES, Belyea BC, Barr FG, and Linardic CM (2013). Human rhabdomyosarcoma cell lines for rhabdomyosarcoma Research: utility and pitfalls. Front. Oncol 3, 1–12. [PubMed: 23373009]

Hsiao TH, Chen HIH, Lu JY, Lin PY, Keller C, Comerford S, Tomlinson GE, and Chen Y (2013). Utilizing-score to identify oncogenic pathways of cholangiocarcinoma. Transl. Cancer Res 2, 6–17. [PubMed: 23905013]

Katoh Y, and Katoh M (2008). Hedgehog signaling, epithelial-to-mesenchymal transition and miRNA. Int. J. Mol. Med 22, 271–275. [PubMed: 18698484]

Khan J, Bittner ML, Saal LH, Teichmann U, Azorsa DO, Gooden GC, Pavan WJ, Trent JM, and Meltzer PS (1999). cDNA microarrays detect activation of a myogenic transcription program by the PAX3-FKHR fusion oncogene. Proc. Natl. Acad. Sci 96, 13264–13269. [PubMed: 10557309]

Kingsbury TJ, Kim MJ, and Civin CI (2019). Regulation of Cancer Stem Cell Properties by SIX1, a Member of the PAX-SIX-EYA-DACH Network (Elsevier Inc.).

Laclef C, Hamard G, Demignon J, Souil E, Houbron C, and Maire P (2003). Altered myogenesis in Six1-deficient mice. Development 130, 2239–2252. [PubMed: 12668636]

Langenau DM, Keefe MD, Storer NY, Guyon JR, Kutok JL, Le X, Goessling W, Neuberg DS, Kunkel LM, and Zon LI (2007). Effects of RAS on the genesis of embryonal rhabdomyosarcoma. Genes Dev 21, 1382–1395. [PubMed: 17510286]

Langmead B, and Salzberg SL (2012). Fast gapped-read alignment with Bowtie 2. Nat. Methods 9, 357–359. [PubMed: 22388286]

Lee EJ, Kim M, Kim YD, Chung MJ, Elfadl A, Ulah HMA, Park D, Lee S, Park HS, Kim TH, et al. (2018). Establishment of stably expandable induced myogenic stem cells by four transcription factors. Cell Death Dis 9, 1092. [PubMed: 30361642]

Leikina E, Gamage DG, Prasad V, Goykhberg J, Crowe M, Diao J, Kozlov MM, Chernomordik LV, and Millay DP (2018). Myomaker and myomerger work independently to control distinct steps of membrane remodeling during myoblast fusion. Dev. Cell 46, 767–780.e7. [PubMed: 30197239]

Leung C, Murad KBA, Tan ALT, Yada S, Sagiraju S, Bode PK, and Barker N (2020). Lgr5 marks adult progenitor cells contributing to skeletal muscle regeneration and sarcoma formation. Cell Rep 33, 108535. [PubMed: 33357435]

Li H, Handsaker B, Wysoker A, Fennell T, Ruan J, Homer N, Marth G, Abecasis G, and Durbin R; 1000 Genome Project Data Processing (2009). The sequence alignment/map format and SAMtools. Bioinformatics 25, 2078–2079. [PubMed: 19505943]

Li S, Chen K, Zhang Y, Barnes SD, Jaichander P, Zheng Y, Hassan M, Malladi VS, Skapek SX, Xu L, et al. (2019). Twist2 amplification in rhabdomyosarcoma represses myogenesis and promotes oncogenesis by redirecting MyoD DNA binding. Genes Dev 33, 626–640. [PubMed: 30975722]

Li X, Oghi KA, Zhang J, Krones A, Bush KT, Glass CK, Nigam SK, Aggarwal AK, Maas R, Rose DW, et al. (2003). Eya protein phosphatase activity regulates Six1–Dach–Eya transcriptional effects in mammalian organogenesis. Nature 426, 247–254. [PubMed: 14628042]

Lin CY, Chen WT, Lee HC, Yang PH, Yang HJ, and Tsai HJ (2009). The transcription factor Six1a plays an essential role in the craniofacial myogenesis of zebrafish. Dev. Biol 331, 152–166. [PubMed: 19409884]

Liu Y, Chakroun I, Yang D, Horner E, Liang J, Aziz A, Chu A, De Repentigny Y, Dilworth FJ, Kothary R, et al. (2013). Six1 regulates MyoD expression in adult muscle progenitor cells. PLoS One 8, e67762. [PubMed: 23840772]

Liu Z, Zhang X, Lei H, Lam N, Carter S, Yockey O, Xu M, Mendoza A, Hernandez ER, Wei JS, et al. (2020). CASZ1 induces skeletal muscle and rhabdomyosarcoma differentiation through a feed-forward loop with MYOD and MYOG. Nat. Commun 11, 911. [PubMed: 32060262]

Lo HW, Hsu SC, Xia W, Cao X, Shih JY, Wei Y, Abbruzzese JL, Hortobagyi GN, and Hung MC (2007). Epidermal growth factor receptor cooperates with signal transducer and activator of transcription 3 to induce epithelial-mesenchymal transition in cancer cells via up-regulation of TWIST gene expression. Cancer Res 67, 9066–9076. [PubMed: 17909010]

Londhe P, and Davie JK (2011). Sequential association of myogenic regulatory factors and E proteins at muscle-specific genes. Skelet. Muscle 1, 14. [PubMed: 21798092]

Lovén J, Hoke HA, Lin CY, Lau A, Orlando DA, Vakoc CR, Bradner JE, Lee TI, and Young RA (2013). Selective inhibition of tumor oncogenes by disruption of super-enhancers. Cell 153, 320–334. [PubMed: 23582323]

MacQuarrie KL, Yao Z, Fong AP, Diede SJ, Rudzinski ER, Hawkins DS, and Tapscott SJ (2013). Comparison of genome-wide binding of MyoD in normal human myogenic cells and rhabdomyosarcomas identifies regional and local suppression of promyogenic transcription factors. Mol. Cell. Biol 33, 773–784. [PubMed: 23230269]

McCoy EL, Iwanaga R, Jedlicka P, Abbey N-S, Chodosh LA, Heichman KA, Welm AL, and Ford HL (2009). Six1 expands the mouse mammary epithelial stem/progenitor cell pool and induces mammary tumors that undergo epithelial-mesenchymal transition. J. Clin. Invest 119, 2663–2677. [PubMed: 19726883]

Menuet A, Pellegrini E, Anglade I, Blaise O, Laudet V, Kah O, and Pakdel F (2002). Molecular characterization of three estrogen receptor forms in zebrafish: binding characteristics, transactivation properties, and tissue Distributions1. Biol. Reprod 66, 1881–1892. [PubMed: 12021076]

Niro C, Demignon J, Vincent S, Liu Y, Giordani J, Sgarioto N, Favier M, Guillet-Deniau I, Blais A, and Maire P (2010). Six1 and Six4 gene expression is necessary to activate the fast-type muscle gene program in the mouse primary myotome. Dev. Biol 338, 168–182. [PubMed: 19962975]

Noguchi YT, Nakamura M, Hino N, Nogami J, Tsuji S, Sato T, Zhang L, Tsujikawa K, Tanaka T, Izawa K, et al. (2019). Cell-autonomous and redundant roles of Hey1 and HeyL in muscle stem cells: HeyL requires HeS1 to bind diverse DNA sites. Development 146, 1–12.

Nord H, Nygård Skalman L, and von Hofsten J (2013). Six1 regulates proliferation of Pax7-positive muscle progenitors in zebrafish. J. Cell Sci 126, 1868–1880. [PubMed: 23444384]

O'Brien JH, Hernandez-Lagunas L, Artinger KB, and Ford HL (2014). MicroRNA-30a regulates zebrafish myogenesis through targeting the transcription factor Six1. J. Cell Sci 127, 2291–2301. [PubMed: 24634509]

Patrick AN, Cabrera JH, Smith AL, Chen XS, Ford HL, and Zhao R (2013). Structure-function analyses of the human SIX1-EYA2 complex reveal insights into metastasis and BOR syndrome. Nat. Struct. Mol. Biol 20, 447–453. [PubMed: 23435380]

Phelps MP, Bailey JN, Vleeshouwer-Neumann T, and Chen EY (2016). CRISPR screen identifies the NCOR/HDAC3 complex as a major suppressor of differentiation in rhabdomyosarcoma. Proc. Natl. Acad. Sci. U. S. A 113, 15090–15095. [PubMed: 27956629]

Pomella S, Sreenivas P, Gryder BE, Wang L, Milewski D, Cassandri M, Baxi K, Hensch NR, Carcarino E, Song Y, et al. (2021). Interaction between SNAI2 and MYOD enhances oncogenesis and suppresses differentiation in Fusion Negative Rhabdomyosarcoma. Nat. Commun 12, 1–15. [PubMed: 33397941]

Qamar L, Deitsch E, Patrick AN, Post MD, Spillman MA, Iwanaga R, Thorburn A, Ford HL, and Behbakht K (2012). Specificity and prognostic validation of a polyclonal antibody to detect Six1 homeoprotein in ovarian cancer. Gynecol. Oncol 125, 451–457. [PubMed: 22333994]

Quinlan AR, and Hall IM (2010). BEDTools: a flexible suite of utilities for comparing genomic features. Bioinformatics 26, 841–842. [PubMed: 20110278]

Ramírez F, Dündar F, Diehl S, Grüning BA, and Manke T (2014). deep-Tools: a flexible platform for exploring deep-sequencing data. Nucleic Acids Res 42, W187–W191. [PubMed: 24799436]

Rekhi B, Gupta C, Chinnaswamy G, Qureshi S, Vora T, Khanna N, and Laskar S (2018). Clinicopathologic features of 300 rhabdomyosarcomas with emphasis upon differential expression of skeletal muscle specific markers in the various subtypes: a single institutional experience. Ann. Diagn. Pathol 36, 50–60. [PubMed: 30098515]

Relaix F, Demignon J, Laclef C, Pujol J, Santolini M, Niro C, Lagha M, Rocancourt D, Buckingham M, and Maire P (2013). Six homeoproteins directly activate myod expression in the gene regulatory networks that control early myogenesis. PLoS Genet 9, e1003425. [PubMed: 23637613]

Robinson MD, McCarthy DJ, and Smyth GK (2010). edgeR: a Bio-conductor package for differential expression analysis of digital gene expression data. Bioinformatics 26, 139–140. [PubMed: 19910308]

Rudnicki MA, Schnegelsberg PNJ, Stead RH, Braun T, Arnold HH, and Jaenisch R (1993). MyoD or Myf-5 is required for the formation of skeletal muscle. Cell 75, 1351–1359. [PubMed: 8269513]

Santolini M, Sakakibara I, Gauthier M, Ribas-Aulinas F, Takahashi H, Sawasaki T, Mouly V, Concordet JP, Defossez PA, Hakim V, et al. (2016). MyoD reprogramming requires Six1 and Six4 homeoproteins: genome-wide cis-regulatory module analysis. Nucleic Acids Res 44, 8621–8640. [PubMed: 27302134]

Shen L, Shao N, Liu X, and Nestler E (2014). ngs.plot: quick mining and visualization of next-generation sequencing data by integrating genomic data-bases. BMC Genomics 15, 284. [PubMed: 24735413]

Shi J, Bi P, Pei J, Li H, Grishin NV, Bassel-Duby R, Chen EH, and Olson EN (2017). Requirement of the fusogenic micropeptide myomixer for muscle formation in zebrafish. Proc. Natl. Acad. Sci. U. S. A 114, 11950–11955. [PubMed: 29078404]

Skene PJ, and Henikoff S (2017). An efficient targeted nuclease strategy for high-resolution mapping of DNA binding sites. Elife 6, e21856. [PubMed: 28079019]

Sokolowski E, Turina CB, Kikuchi K, Langenau DM, and Keller C (2014). Proof-of-concept Rare Cancers in Drug Development: The Case for Rhabdomyosarcoma. Oncogene 33, 1877–1889. [PubMed: 23665679]

Soleimani VD, Yin H, Jahani-Asl A, Ming H, Kockx CEM, van Ijcken WFJ, Grosveld F, and Rudnicki MA (2012). Snail regulates MyoD binding-site occupancy to direct enhancer switching and differentiation-specific transcription in myogenesis. Mol. Cell 47, 457–468. [PubMed: 22771117]

Spitz F, Demignon J, Porteu A, Kahn A, Concordet JP, Daegelen D, and Maire P (1998). Expression of myogenin during embryogenesis is controlled by Six/sine oculis homeoproteins through a conserved MEF3 binding site. Proc. Natl. Acad. Sci. U. S. A 95, 14220–14225. [PubMed: 9826681]

Subramanian A, Tamayo P, Mootha VK, Mukherjee S, Ebert BL, Gillette MA, Paulovich A, Pomeroy SL, Golub TR, Lander ES, et al. (2005). Gene set enrichment analysis: a knowledge-based approach for interpreting genome-wide expression profiles. Proc. Natl. Acad. Sci. U. S. A 102, 15545–15550. [PubMed: 16199517]

Talbot JC, Teets EM, Ratnayake D, Duy PQ, Currie PD, and Amacher SL (2019). Muscle precursor cell movements in zebrafish are dynamic and require six-family genes. Development 146, dev171421. [PubMed: 31023879]

Tenente IM, Hayes MN, Ignatius MS, McCarthy K, Yohe M, Sindiri S, Gryder B, Oliveira ML, Ramakrishnan A, Tang Q, et al. (2017). Myogenic regulatory transcription factors regulate growth in rhabdomyosarcoma. Elife 6, e19214. [PubMed: 28080960]

Thisse B, Heyer V, Lux A, Alunni V, Degrave A, Seiliez I, Kirchner J, Parkhill J-P, and Thisse C (2004). Spatial and temporal expression of the ze-brafish genome by large-scale in situ hybridization screening. In The Zebrafish: Genetics, Genomics, and Informatics (Academic Press), pp. 505–519.

Weintraub H, Tapscott SJ, Davis RL, Thayer MJ, Adam MA, Lassar AB, and Miller AD (1989). Activation of muscle-specific genes in pigment, nerve, fat, liver, and fibroblast cell lines by forced expression of MyoD. Proc. Natl. Acad. Sci. U. S. A 86, 5434–5438. [PubMed: 2748593]

Whyte WA, Orlando DA, Hnisz D, Abraham BJ, Lin CY, Kagey MH, Rahl PB, Lee TI, and Young RA (2013). Master transcription factors and mediator establish super-enhancers at key cell identity genes. Cell 153, 307–319. [PubMed: 23582322]

Wu W, Ren Z, Zhang L, Liu Y, Li H, and Xiong Y (2013). Overexpression of Six1 gene suppresses proliferation and enhances expression of fast-type muscle genes in C2C12 myoblasts. Mol. Cell. Biochem 380, 23–32. [PubMed: 23613228]

Wu W, Huang R, Wu Q, Li P, Chen J, Li B, and Liu H (2014). The role of Six1 in the genesis of muscle cell and skeletal muscle development. Int. J. Biol. Sci 10, 983–989. [PubMed: 25210496]

Yajima H, Motohashi N, Ono Y, Sato S, Ikeda K, Masuda S, Yada E, Kanesaki H, Miyagoe-Suzuki Y, Takeda S, et al. (2010). Six family genes control the proliferation and differentiation of muscle satellite cells. Exp. Cell Res 316, 2932–2944. [PubMed: 20696153]

Yang Z, MacQuarrie KL, Analau E, Tyler AE, Dilworth FJ, Cao Y, Diede SJ, and Tapseott SJ (2009). MyoD and E-protein heterodimers switch rhabdomyosarcoma cells from an arrested myoblast phase to a differentiated state. Genes Dev 23, 694–707. [PubMed: 19299559]

Yu G, Wang LG, Han Y, and He QY (2012). ClusterProfiler: an R package for comparing biological themes among gene clusters. Omi. A. J. Integr. Biol 16, 284–287.

Yu G, Wang LG, and He QY (2015). ChIP seeker: an R/Bioconductor package for ChIP peak annotation, comparison and visualization. Bioinformatics 31, 2382–2383. [PubMed: 25765347]

Yu Y, Khan J, Khanna C, Helman L, Meltzer PS, and Merlino G (2004). Expression profiling identifies the cytoskeletal organizer ezrin and the developmental homeoprotein Six-1 as key metastatic regulators. Nat. Med 10, 175–181. [PubMed: 14704789]

Yu Y, Davicioni E, Triche TJ, and Merlino G (2006). The homeoprotein Six1 transcriptionally activates multiple protumorigenic genes but requires ezrin to promote metastasis. Cancer.Res 66, 1982–1989. [PubMed: 16488997]

Zammit PS (2017). Function of the myogenic regulatory factors Myf5, MyoD, Myogenin and MRF4 in skeletal muscle, satellite cells and regenerative myogenesis. Semin. Cell Dev. Biol 72, 19–32. [PubMed: 29127046]

Zhang Y, Liu T, Meyer CA, Eeckhoute J, Johnson DS, Bernstein BE, Nussbaum C, Myers RM, Brown M, Li W, et al. (2008). Model-based analysis of ChIP-seq (MACS). Genome Biol 9, R137. [PubMed: 18798982]

Zhou H, Blevins MA, Hsu JY, Kong D, Galbraith MD, Goodspeed A, Culp-Hill R, Oliphant MUJ, Ramirez D, Zhang L, et al. (2020). Identification of a small-molecule inhibitor that disrupts the SIX1/EYA2 complex, EMT, and metastasis. Cancer Res 80, 2689–2702. [PubMed: 32341035]

Zhou X, Maricque B, Xie M, Li D, Sundaram V, Martin EA, Koebbe BC, Nielsen C, Hirst M, Farnham P, et al. (2011). The human Epigenome browser at Washington university. Nat. Methods 8, 989–990. [PubMed: 22127213]

Highlights

- FN-RMS tumors are highly dependent on SIX1 for growth
- In RMS, SIX1 enhances open chromatin at stem/oncogenic superenhancers
- SIX1 KD reprograms MYOD1 to occupy muscle differentiation rather than stem loci
- A gene signature derived from SIX1 loss is predictive of advanced RMS

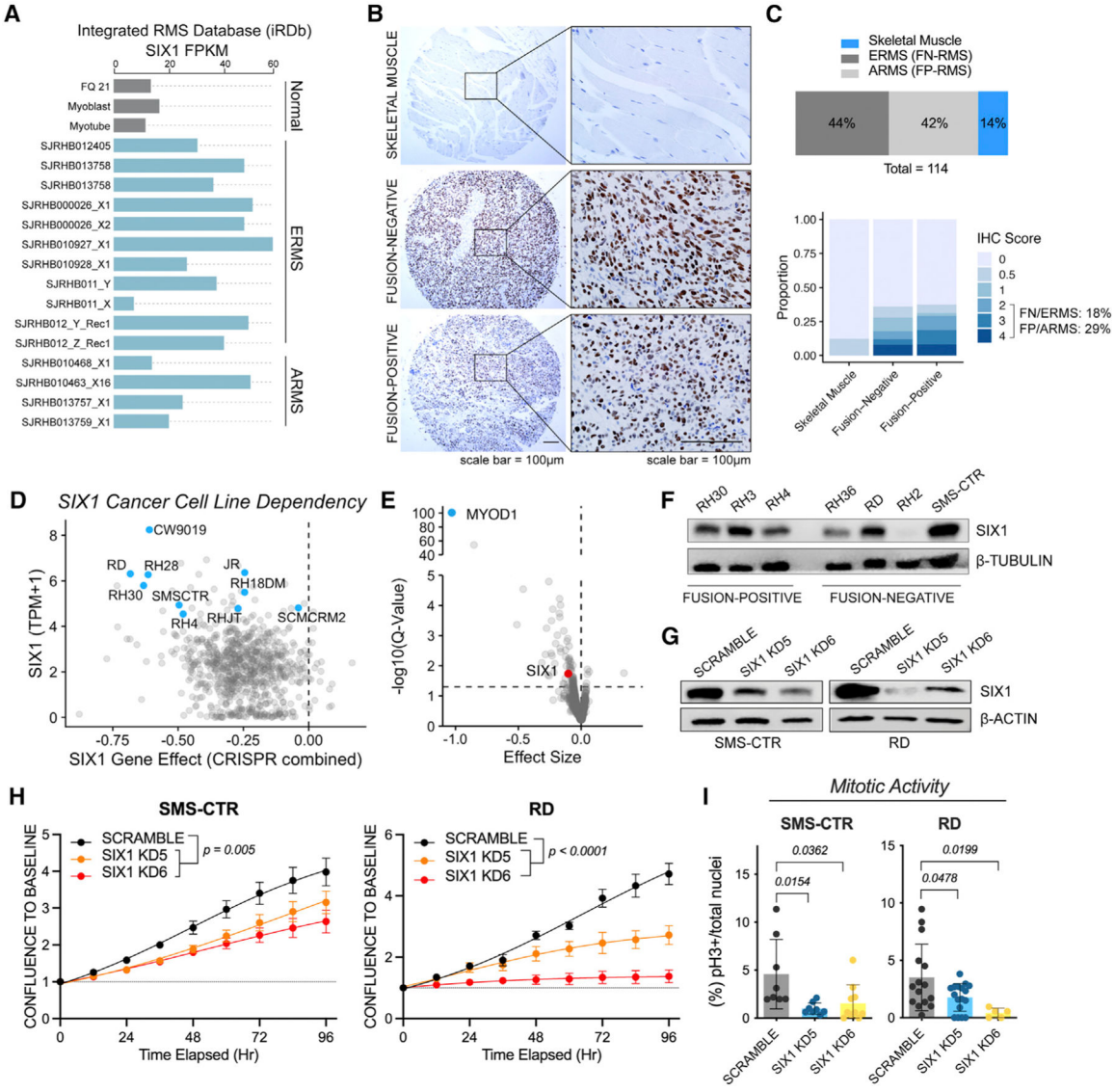

Figure 1. SIX1 is overexpressed and predicted to be an essential gene in RMS

(A) Fragments per kilobase million (FPKM) for SIX1 in the St. Jude Pediatric Cancer Genome Project cohort (gray, normal skeletal muscle controls; FQ21, fetal quadriceps muscle).

(B) IHC staining (DAB) for SIX1 on an RMS tissue array containing normal skeletal muscle controls. The array was counterstained with hematoxylin.

(C) Distribution of samples on the RMS and skeletal muscle tissue arrays (top) and distribution of IHC scores (bottom).

(D) SIX1 transcripts per kilobase million (TPM) plotted against the SIX1 gene effect score in 1,775 cell lines in the Cancer Dependency Map CRISPR-Cas9 KO screen (blue dots, RMS).

(E) Volcano plot of gene dependency scores for MYOD1 (blue) and SIX1 (red) in RMS cell lines versus all other cell lines. Statistical analysis was performed using a two-class Kolmogorov-Smirnov test.

(F) Western blot analysis of SIX1 across a panel of FN and FP RMS human cell lines.
(G) Western blot analysis of SIX1 KD in RD and SMS-CTR cell lines. Representative KDs are shown.
(H) IncuCyte live-cell imaging growth assays of SMS-CTR and RD Scramble and SIX1 KD cells over 96 h. Cells were plated in triplicate, and relative cell growth was measured by normalizing confluency at each time point relative to initial confluency. Data represent mean ± SD from one representative experiment at each time point, and statistical differences between Scramble and SIX1 KD5 or KD6 were measured by fitting data to a longitudinal mixed-effects model.
(I) Mitotic activity of SMS-CTR and RD Scramble and SIX1 KD cells measured by pH3 staining and DAPI counterstaining; each dot represents data from one independent experiment.

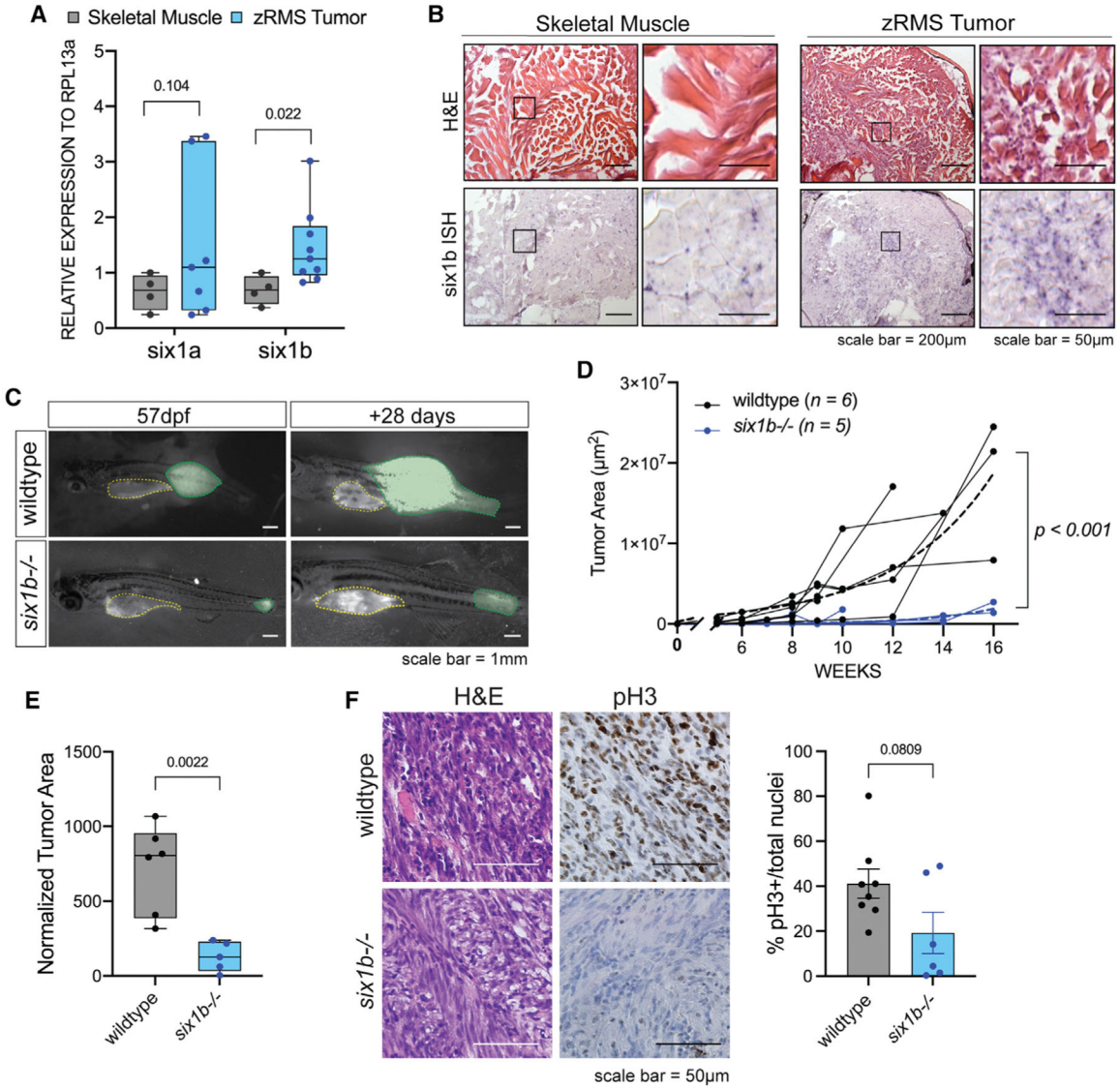

Figure 2. *six1b* is required for zebrafish RMS growth

(A) Quantitative real-time PCR for *six1a* and *six1b* in dissected GFP+ zRMS tissue compared with age-matched normal skeletal muscle (n = 4 normal muscle samples, n = 6 zRMS samples).

(B) Representative images of *six1b* transcripts as visualized by H&E and ISH (n = 5 fish per group).

(C) Representative images of tumor progression (colored in green) from 57–85 dpf in wild-type and *six1b*$^{-/-}$ siblings. The yellow outline represents autofluorescence from the stomach.

(D)Quantification of GFP+ tumor area in each fish over time. Tumor growth is represented as individual tracks. Composite growth of wild-type and *six1b*$^{-/-}$ tumors was fitted to a non-linear logistical growth model and is represented by dotted lines. A longitudinal mixed-effects model was used to measure statistical differences.

(E) Tumor area normalized to standard length of fish at 120 dpf or earlier time points because of moribundity. Statistical differences were calculated using Welch's t test.
(F) Representative staining and quantification of H&E and pH3 IHC in sectioned zRMS tumors. Dots in the graph represent the percentage of pH3 staining/tumor section; staining was quantified over 2 sections/tumor (n = 4 wild-type [WT] tumors, n = 3 *six1b*$^{-/-}$ tumors). Statistical differences were calculated using Welch's t test.

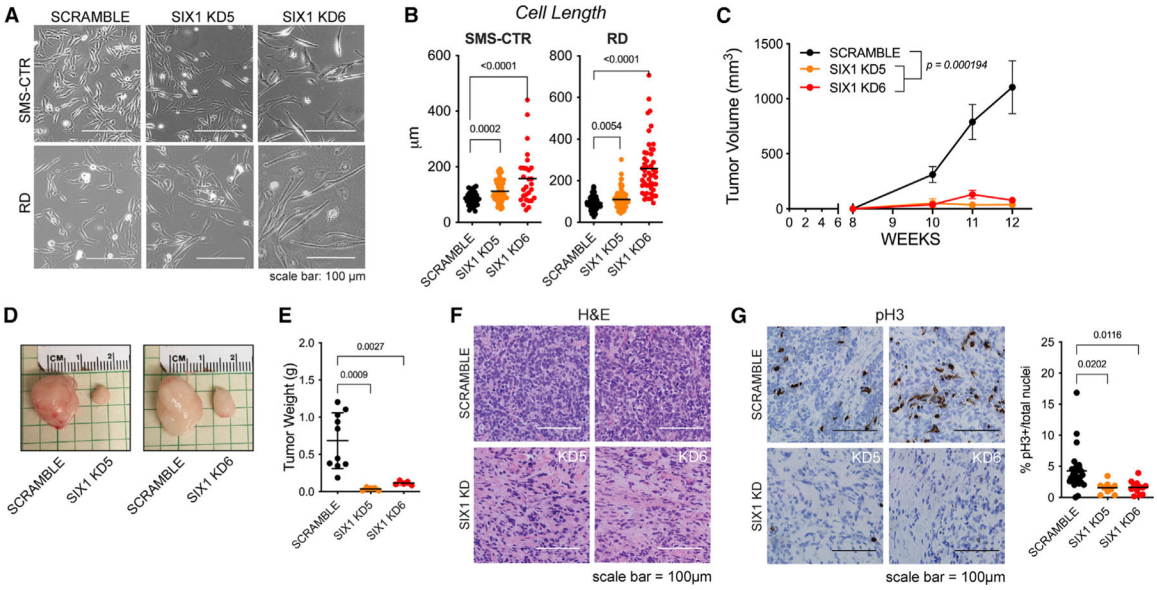

Figure 3. SIX1 KD inhibits human RMS growth and progression

(A and B) Bright-field images depicting the elongated cell morphology of SIX1 KD SMS-CTR and RD cells (A) and quantification of cell length (B). Statistical differences were calculated using one-way ANOVA followed by Dunnett's multiple comparisons post hoc test.

(C) Tumor volumes, measured by caliper, over 12-weeks for Scramble and SIX1 KD SMS-CTR cells that were engrafted into the flanks of NSG mice. Data were fitted to a longitudinal mixed-effects model for statistical analysis of Scramble and SIX1 KD samples. Error bars represent mean ± SD at each time point.

(D) Representative images of dissected Scramble or SIX1 KD xenografted tumors at 12 weeks.

(E) Final tumor weights in grams at the end of the study (n = 10 mice total). Statistical differences were calculated using one-way ANOVA followed by Dunnett's multiple comparisons post hoc test.

(F) Representative H&E histology of dissected Scramble and SIX1 KD xenografted tumors (n = 5 tumors/KD).

(G) Representative pH3 immunostaining (brown) of dissected Scramble and SIX1 KD xenografted tumors. Dots in the graph represent the percentage of pH3+ cells per tumor section; pH3 staining was quantified over 2 sections per tumor. Statistical differences were calculated using one-way ANOVA followed by Dunnett's multiple comparisons post hoc test.

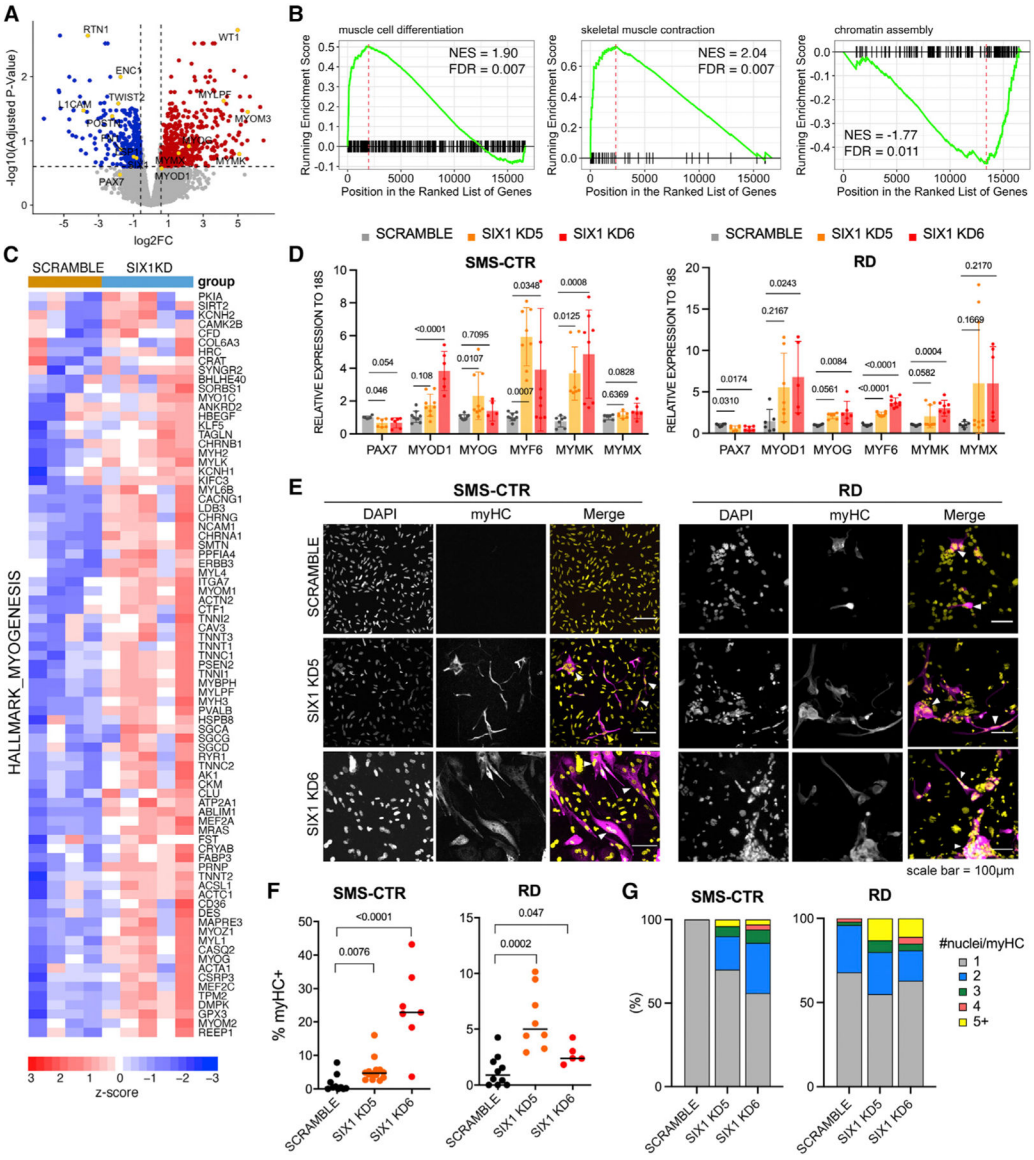

Figure 4. SIX1 KD induces myogenic differentiation in RMS cells

(A) Volcano plot of $\log_2$ fold change (log2FC) gene expression (SIX1 KD over Scramble) and adjusted p value after differential expression analysis from SMS-CTR RNA-seq. Red and blue dots denote genes significantly upregulated and downregulated upon SIX1 KD, respectively.

(B) GSEA plots of ranked log2FC expression (SIX1 KD over Scramble) show positive enrichment for curated muscle cell differentiation and skeletal muscle contraction gene signatures and negative enrichment for chromatin assembly gene signatures.

(C) Heatmap expression of the Molecular Signatures DataBase (MSigDB) myogenesis gene set across Scramble and SIX1 KD samples. Scale bar represents *Z* score-converted log2CPM values.

(D) qRT-PCR of genes involved in muscle differentiation in SMS-CTR and RD cell lines with SIX1 KD. Each dot represents one independent biological replicate. Statistical

differences were calculated using one-way ANOVA followed by post hoc Dunnett's multiple comparisons test.

(E) MyHC (magenta) immunostaining and DAPI counterstain (yellow) in SIX1 KD RMS cells compared with Scramble RMS cells.

(F) Quantification of myHC staining over total nuclei per field of view; each dot represents the percentage of myHC+ cells over one technical replicate from at least 3 independent experiments.

(G)Fusion indices of SMS-CTR and RD control and SIX1 KD cells. Statistical differences were calculated by one-way ANOVA followed by Dunnett's multiple comparisons post hoc test.

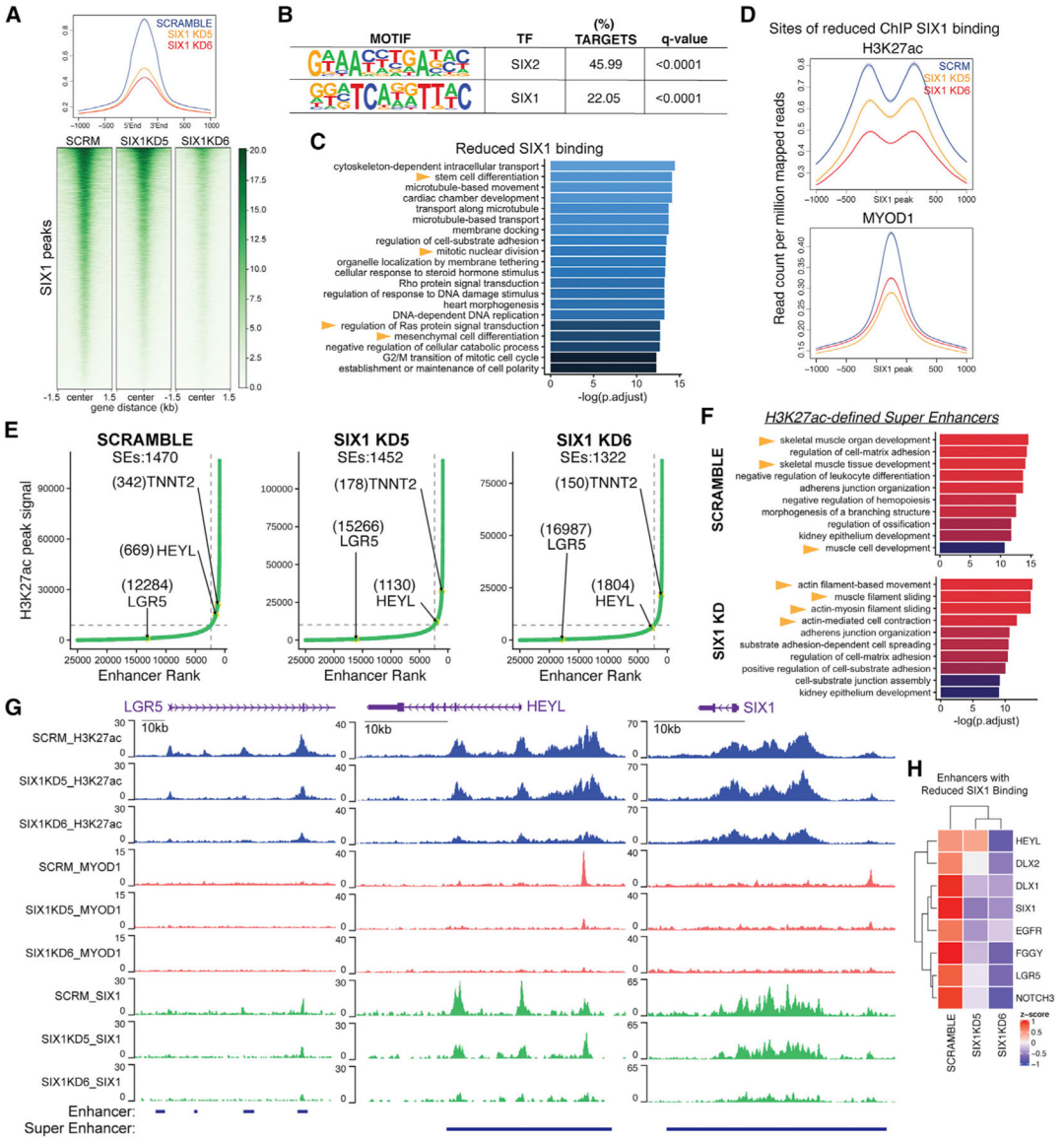

Figure 5. SIX1 globally regulates stem/oncogenic and myogenic differentiation genes through fine-tuning of SE activity

(A) Heatmaps and average profiles of genome-wide SIX1 ChIP-seq signals in SMS-CTR Scramble and SIX1 KD5 and KD6 cells, centered at Scramble SIX1 peaks.

(B) Motif analysis of peak coordinates exhibiting 1.5-fold reduced SIX1 binding in SIX1 KD5 and KD6 SMS-CTR SIX1 ChIP-seq datasets. The top 2 enriched motifs are shown.

(C)Pathway enrichment of annotated sites of SIX1 loss in SIX1 KD5 and KD6 lines.

(D)Average profiles of MYOD1 and H3K27ac ChIP signal over loci that exhibited 1.5-fold reduced SIX1 binding in SIX1 KD cells compared with Scramble cells.

(E) ROSE analysis performed on Scramble and SIX1 KD H3K27ac peaks shows a shift in *HEYL* (down) and *TNNT2/TNNI1* (up) superenhancer (SE) rank between Scramble and SIX1 KD cells. Ranks of SEs are labeled in parentheses next to the annotated SE.

(F) Pathway enrichment of genes associated with SEs identified in Scramble and the union of SEs identified in SIX1 KD5 and KD6 (SIX1 KD) cells.

(G) H3K27ac, MYOD1, and SIX1 ChIP signal over the *LGR5*, *HEYL*, and *SIX1* enhancers. (H) CPM expression of example SE-regulated genes with known stem cell functions that exhibited at least 1.5-fold SIX1 reduced binding, taken from RNA-seq comparing SCRM and SIX1 KD cells.

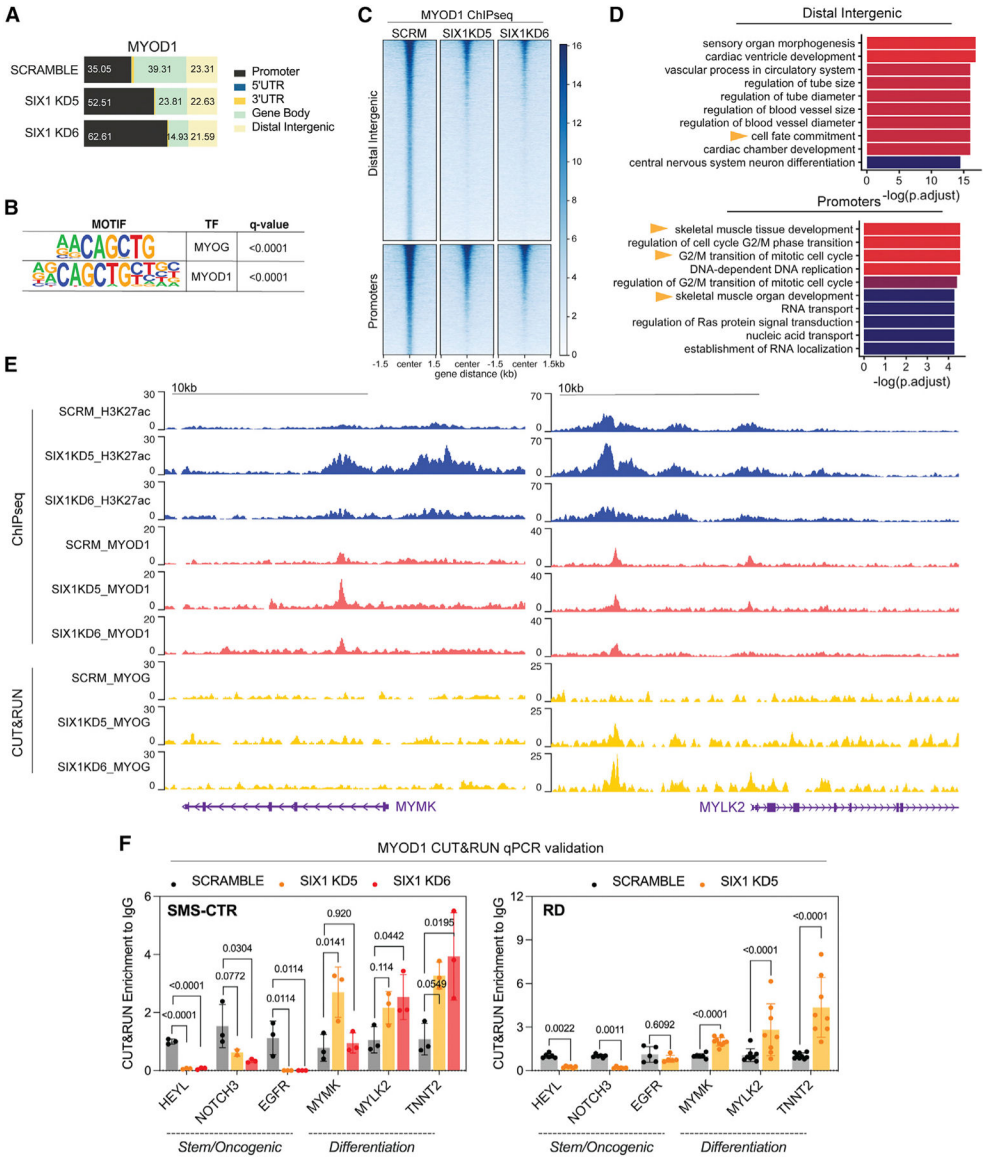

Figure 6. SIX1 loss alters MYOD1 occupancy at muscle differentiation and stem/oncogenic loci

(A) Peak distribution of the MYOD1 TF in SMS-CTR Scramble and SIX1 KD5 and KD6 cells across promoters (±2.5 kb from annotated TSSs), 5′/3′ UTR, gene body (which includes intronic and exonic regions), and distal intergenic/enhancer regions.

(B) Motif analysis of overlapping macs2 MYOD1 peak coordinates; the top 2 motifs are shown.

(C) Heatmaps of MYOD1 signal at annotated MYOD1-bound distal intergenic and promoter regions.

(D) Pathway enrichment of distal intergenic and promoter-bound MYOD1 peaks.

(E) H3K27ac, MYOD1, and MYOG tracks over the *MYMK* and *MYLK2* loci in SIX1 KD and Scramble SMS-CTR cells.

(F) C&R quantitative real-time PCR validation of changes in MYOD1 binding at stem/oncogenic and myogenic differentiation genes that occur in SMS-CTR and RD SIX1 KD

cells. Statistical differences for each loci were measured using one-way ANOVA followed by post hoc Dunnett's multiple comparisons test.

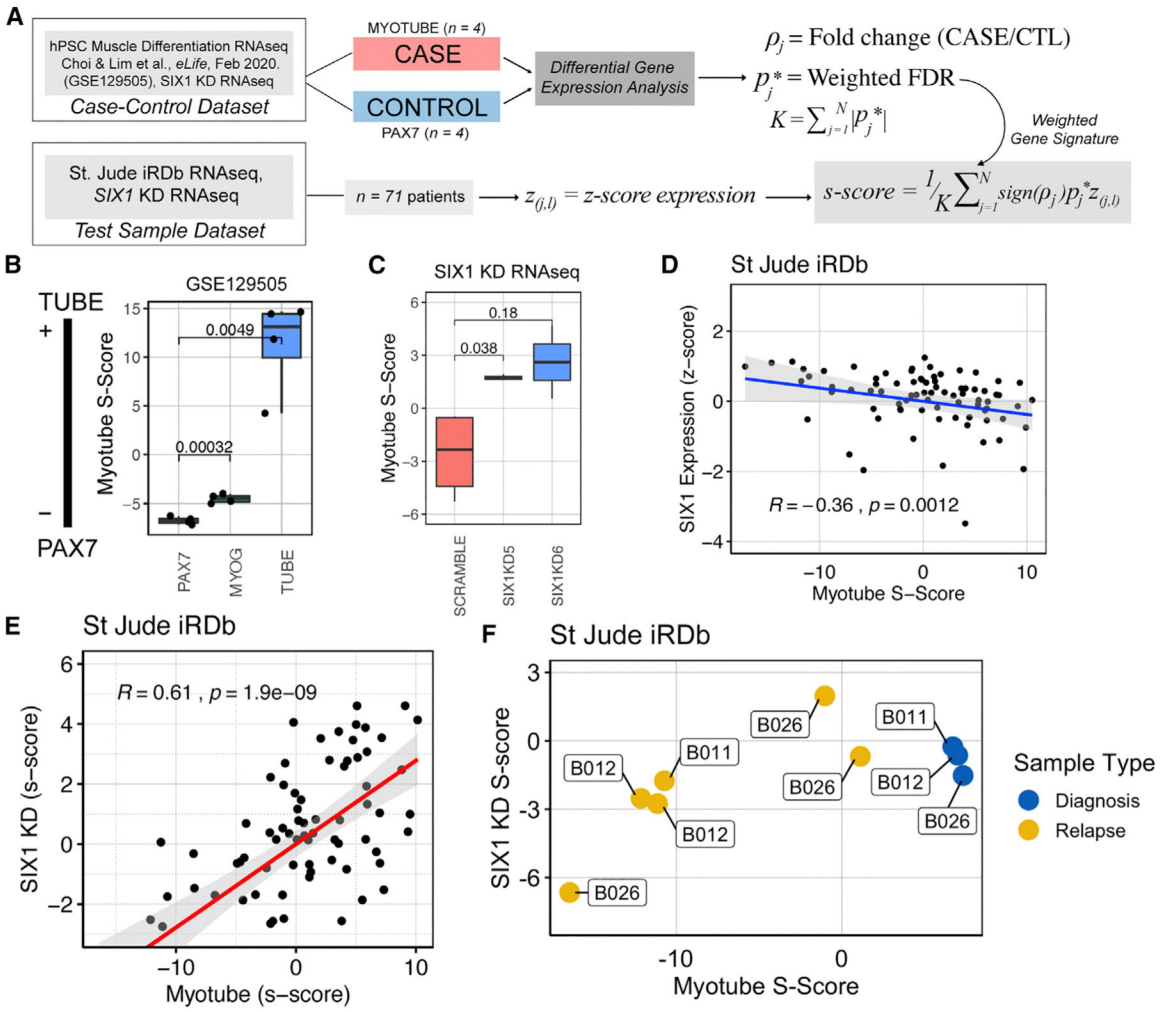

Figure 7. SIX1 expression in RMS patients is inversely correlated with a myotube gene signature

(A) Overview of the *S* scoring methodology, where gene expression in the case-control data is used to generate a weighted gene signature to score test sample transcriptomes on a continuous scale.

(B) Myotube *S* scores for samples used in the training set plotted as proof of concept that the myotube *S* score can quantify myogenic differentiation status. Statistical differences were measured by Student's t test.

(C) Myotube *S* scoring methodology applied to the SIX1 KD RNA-seq dataset, demonstrating that SIX1 KD cells are more advanced in the myogenic lineage than Scramble cells. Statistical differences were measured by Student's t test.

(D) Scatterplot of myotube *S* scores plotted against SIX1 *Z* score-converted expression and Spearman rank correlation coefficient show a moderate inverse correlation between differentiation status and SIX1 expression in St. Jude RMS samples (n = 71).

(E) Scatterplot of SIX1 KD *S* scores derived from SIX1 KD RNA-seq data against myotube *S* score shows a strong positive correlation between the SIX1 KD and myotube gene signatures in the St. Jude RMS dataset.

(F) Myotube and SIX1 KD *S* scores of three individuals, with biopsies collected at multiple stages of disease.

KEY RESOURCES TABLE

REAGENT or RESOURCE	SOURCE	IDENTIFIER
Antibodies		
Mouse monoclonal anti-SIX1 (1229, 992)	In-house purified antibody	N/A
Rabbit polyclonal anti-SIX1	Atlas Antibodies	HPA0011893; AB_1079991
Rabbit polyclonal anti-H3K27ac	Abcam	ab4729; AB_2118291
Rabbit monoclonal anti-MYOD1	Abcam	ab133627; AB_2890928
Mouse monoclonal anti-MYOG	Abcam	ab1835; AB_302633
Mouse monoclonal anti-myosin heavy chain	DSHB	MF-20; AB_2147781
Mouse monoclonal anti-PAX7	DSHB	PAX7; AB_528428
Rabbit polyclonal anti-pH3 (pSer10)	Sigma-Aldrich	H0412; AB_477043
Rabbit polyclonal anti-cleaved caspase 3	Cell Signaling Technology	9661; AB_2341188
Normal Rabbit IgG	Cell Signaling Technology	2729; AB_1031062
Mouse β-TUBULIN	Sigma-Aldrich	T4026; AB_477577
Mouse β-ACTIN	Sigma-Aldrich	A5316; AB_476743
Mouse β-ACTIN-HRP	Abcam	ab49900; AB_867494
Bacterial and virus strains		
Subcloning Efficiency DH5α competent cells	ThermoFisher	18265017
Biological samples		
Rhabdomyosarcoma with striated muscle tumor array	Biomax	SO2082b
Chemicals, peptides, and recombinant proteins		
Polybrene	Millipore	TR-1003
Phenol-red solution	Sigma	P0290
Puromycin Dihydrochloride	Research Products Int.	P33020
pAG-MNase	EpiCypher	15–1116
Fugene Transfection Reagent	Promega	E2311
Tricaine (MS-222)	Sigma Aldrich	A5040
ECL Western blot substrate	Pierce	32106
Digitonin	Millipore Sigma	30–041
Spermidine	Sigma Aldrich	S0266
Critical commercial assays		
MycoAlert detection kit	Lonza	LT07–418
Direct-zol RNA prep kit	Zymo Research	R2052
iScript reverse transcription kit	Bio-Rad	1708841
SsoFast EvaGreen supermix	Bio-Rad	1725205
Verso cDNA synthesis kit	ThermoFisher	AB-1453A
Taqman gene expression master mix	Applied Biosystems	4369542

REAGENT or RESOURCE	SOURCE	IDENTIFIER
Nuclei EZ prep kit	Sigma Aldrich	NUC101
Dynabeads Antibody Coupling kit	ThermoFisher	14311D
Concavalin A beads	EpiCypher	21–1401
Universal Plus mRNA-Seq library prep kit	Nugen	0508
KAPA HyperPrep ChIP library kit	Roche	KK8502
NEBNext II Ultra library prep kit	NEB	E7645, E7600S
DNA Clean and Concentrator kit	Zymo Research	D4033
Deposited data		
SIX1 KD RNAseq	This paper	GEO: GSE173155
SIX1, MYOD1, H3K27ac ChIPseq	This paper	GEO: GSE173155
Pan-Sarcoma and normal tissue expression	Downloaded from Oncogenomics database	https://fsabcl-pob01p.ncifcrf.gov/cgi-bin/JK
Pediatric Sarcoma expression	Downloaded from St. Jude PeCAN portal	https://pecan.stjude.cloud/proteinpaint/study/pan-target
Rhabdomyosarcoma patient RNAseq	Downloaded from St. Jude Integrated RMS Database	https://pecan.stjude.cloud/proteinpaint/study/RHB2018
hPSC muscle differentiation RNAseq	(Choi et al., 2020)	GSE129505
Experimental models: cell lines		
HEK293T	ATCC	CVCL_0063
Human: RH30	Mark Hatley (Hanna et al., 2018)	CVCL_0041
Human: RH3 (RH28)	Mark Hatley	CVCL_L415
Human: RH4	Mark Hatley	CVCL_5916
Human: RD	Mark Hatley	CVCL_1649
Human: RH36	Mark Hatley	CVCL_M599
Human: RH2	Mark Hatley	CVCL_A460
Human: SMS-CTR	Mark Hatley	CVCL_A770
Human: SMS-CTR stable Scramble	This paper	N/A
Human: SMS-CTR stable shSIX1 KD5	This paper	N/A
Human: SMS-CTR stable shSIX1 KD6	This paper	N/A
Human: RD stable Scramble	This paper	N/A
Human: RD stable shSIX1 KD5	This paper	N/A
Human: RD stable shSIX1 KD6	This paper	N/A
Experimental models: organisms/strains		
Zebrafish: AB	ZIRC	ZL1
Zebrafish: *six1b*^{oz1}	Sharon Amacher (Talbot et al., 2019)	N/A
Mouse: NOD/SCIDγ	CU AMC Breeding Core	N/A
Oligonucleotides		
For SYBR CUT&RUN primer sequences, see Table S2	This paper	N/A
For SYBR CUT&RUN primer sequences, see Table S2	This paper	N/A

REAGENT or RESOURCE	SOURCE	IDENTIFIER
For Taqman Primer/Probe sequences, see Table S3	This paper	N/A
Recombinant DNA		
rag2-KRASG12D	(Langenau et al., 2007)	N/A
rag2-eGFP	(Langenau et al., 2007)	N/A
pLKO.1-shSIX1 KD5 (3′UTR)	Functional Genomics Core	TRCN0000015233
pLKO.1-shSIX1 KD6 (CDS)	Functional Genomics Core	TRCN0000015236
pLKO.1-Scramble	Addgene	1864
Software and algorithms		
FastQC	Babraham Bioinformatics	https://www.bioinformatics.babraham.ac.uk/projects/
BBDuk	Joint Genome Institute	http://jgi.doe.gov/data-and-tools/bb-tools
STAR	(Dobin et al., 2013)	http://code.google.com/p/rna-star/
edgeR	(Robinson et al., 2010)	https://bioconductor.org/packages/edgeR
clusterProfiler	(Yu et al., 2012)	https://bioconductor.org/packages/clusterProfiler
RCisTarget	(Aibar et al., 2017)	https://bioconductor.org/packages/RcisTarget
Bowtie2 (v.2.3.4.3)	(Langmead and Salzberg, 2012)	http://bowtie-bio.sourceforge.net/bowtie2/index.shtml
Samtools (v.1.11)	(Li et al., 2009)	http://www.htslib.org/
Picard	Broad Institute	http://broadinstitute.github.io/picard/
Bedtools	(Quinlan and Hall, 2010)	https://github.com/arq5x/bedtools2/releases
MACS2	(Zhang et al., 2008)	https://pypi.org/project/MACS2/
ChIPseeker	(Yu et al., 2015)	https://bioconductor.org/packages/ChIPseeker/
ngs.plot	(Shen et al., 2014)	https://github.com/shenlab-sinai/ngsplot
deepTools	(Ramírez et al., 2014)	https://github.com/deeptools
HOMER (v.4.11)	(Heinz et al., 2010)	http://homer.ucsd.edu/homer/
Rank Ordering of Super Enhancers (ROSE)	(Lovén et al., 2013; Whyte et al., 2013)	http://younglab.wi.mit.edu/super_enhancer_code.html
Python version 3.8	Python	https://www.python.org/
FIJI	ImageJ	http://imagej.nih.gov/ij
Prism 9	GraphPad	www.graphpad.com
IGV 2.8.0	Broad Institute	https://software.broadinstitute.org/software/igv/2.8.x
Signature Scoring Algorithm (*S*-score)	(Hsiao et al., 2013)	https://github.com/jywhsu/weighted-genesig-scoring
Other		
Nunc LabTek Chamber Slide System	ThermoFisher	154526PK
DNA LoBind Microcentrifuge tubes	Eppendorf	13–698-790